MODELING AND ANALYSIS OF HYDRAULIC FRACTURE SKIN AND ITS CONTROL

ON SHALE GAS PRODUCTION FROM HORIZONTAL WELLS

A Thesis

by

GRACE PEPE ATAMA

Submitted to the Graduate and Professional School of
Texas A&M University
in partial fulfillment of the requirements for the degree of

MASTER OF SCIENCE

Chair of Committee,	I. Yucel Akkutlu
Committee Members,	Eduardo Gildin
	Frederick Chester
Head of Department,	Jeff Spath

May 2022

Major Subject: Petroleum Engineering

ABSTRACT

It is widely recognized that hydraulic fracturing creates a region of altered permeability near the fracture/matrix interface. Although we have a limited understanding, it is believed this region plays an important role on the production rates. The objective of this study is to model the region as a fracture skin explicitly including local physical and chemical phenomena and their associated effects, namely: (1) permeability improvement due to unpropped fracture development during the fracturing, (2) stress increase due to slick water invasion and clay-swelling effect developing after the fracturing, and (3) water-saturation buildup due to capillary end effect (CEE) developing during the flowback and production. A sensitivity analysis on the derived skin indicates key parameters controlling production and help in minimizing the damage.

In order to develop the hydraulic fracture skin model, two cases are considered: In Case 1, gas flow occurs without any alterations in the formation (no skin), whereas Case 2 considers gas flow occurs in a region near the hydraulic fracture/matrix interface in the presence of the alterations. The difference in the derived pressure drop between the two cases (i.e., Case 2 minus Case 1) is the total pressure drop due to the three combined effects. Improvement in permeability is introduced in Case 2 using a stress-sensitive matrix permeability model. This model considers the presence of unpropped fractures and cracks in the altered zone. Formation damage due to CEE is introduced by defining a new associated gas relative permeability, while damage due to clay swelling is introduced by adding an osmotic pressure term into the permeability model.

The proposed fracture skin increases at a decreasing rate with distance away from the fracture/matrix interface, which mirrors the invaded fracturing fluid (slick-water) near the interface. The sensitivity analysis performed shows that clay swelling is the predominant damage mechanism and is controlled by the geo-mechanical parameters of the permeability model: (i) the

normalized effective stress at the fracture matrix/interface when clay swelling develops in the altered zone, and (ii) strength of the unpropped fractures and cracks inside the damage zone to stay open. On the other hand, the contribution of CEE to the skin is mainly controlled by the average water saturation in the damaged zone. CEE can thus be severe in formations with high water saturation. To minimize the damage, the salinity of the injected water needs to be increased, which in turn will reduce the chemical imbalance between the clay-bound water and slick-water, preventing osmosis. In addition, using proppants with a wider particle size distribution could reduce the damage by allowing smaller size proppants to invade into these secondary fractures and cracks, hence, keeping them propped open during the production.

The hydraulic fracture skin model can be used with the commercial simulators. In this thesis, using Eclipse, I show that the model helps to gain a significantly improved understanding of the alterations induced by the fracturing fluid invasion. This improved understanding will help in minimizing the damage and will ensure optimum benefits of improved productivity.

The literature addresses the issues related to wellbore skin in-depth but the wellbore skin is negligible in unconventional wells and it is the hydraulic fracture skin that counts during the production of oil and gas using horizontal wells with multi-stage fractures. In the latter case, the total fracture surface area of the well could be in the order of hundred acres. An incorrect description of the skin enveloping this large area could be critical in analyzing production trends and optimizing the well performance. The skin is incorrectly identified by the industry as the "stimulated zone", not considering the impact of water invasion on the transport. This article is the first documented effort looking into the hydraulic fracture skin in a systematic fashion considering its multi-physics nature.

My work focusses on shale gas wells. It is important that the analysis and discussion is extended into shale oil/condensate wells. Intuitively, one would expect that these effects persist during oil and gas multi-phase flow because the problem is still drainage of water during the production leading to CEE, whereas the clay swelling is a phenomenon independent of the hydrocarbons. However, it should be recognized that clay swelling is less pronounced in gas reservoir because of their high thermal maturity and compaction, which reduces clay-bound water.

ACKNOWLEDGEMENTS

I would like to thank my committee chair, Dr. I. Yucel Akkutlu, and my committee members, Dr. Eduardo Gildin and Dr. Frederick Chester, for their guidance and support throughout the course of this research.

Thanks also go to my friends and colleagues and the department faculty and staff for making my time at Texas A&M University a memorable experience.

Finally, thanks to my family for their love, encouragement and support during my graduate studies.

CONTRIBUTORS AND FUNDING SOURCES

Contributors

This work was supervised by a thesis committee consisting of Dr. I. Yucel Akkutlu [advisor] and Dr. Eduardo Gildin of the Department of Petroleum Engineering and Dr. Frederick Chester of the Department of Geology and Geophysics.

All work for the thesis was completed independently by the student.

Funding Sources

NOMENCLATURE

a   Gradient of the normalized effective stress $[\text{ft}^{-1}]$

A Fracture cross-sectional area $[\text{ft}^2]$

A_{CEE} Effective fracture cross-sectional area in the altered zone $[\text{ft}^2]$

A_e Effective fracture cross-sectional area in the water invaded zone $[\text{ft}^2]$

b   Normalized effective stress at the matrix/fracture interface in the absence of alterations in the reservoir.

c   Gradient of the normalized effective stress in the altered zone $[\text{ft}^{-1}]$

d   Normalized effective stress at the matrix/fracture interface in the presence of alterations in the reservoir.

h   Fracture height [ft]

K   Stress-sensitive matrix permeability outside the altered zone [md]

K_{clay} Stress-sensitive permeability in the altered zone [md]

K_0 Matrix permeability at zero effective stress [md]

K_s Improved matrix permeability in the altered zone at zero effective stress [md]

k_{rg} Gas relative permeability outside the altered zone

$k_{rg,CEE}$ Gas relative permeability in the altered zone

$\overline{k_{rg,CEE}}$ Average gas relative permeability in the altered zone

L   Length of the water invaded zone [ft]

L_u End of the water invaded zone [ft]

L_d End of the altered zone [ft]

m   Strength of the pore to hold the aperture open

M_s Salt molar mass [Kg/mol]

P_0 Effective stress at zero permeability [psi]

P_1 Pore pressure at the fracture/matrix interface in the absence of alterations in the reservoir [psi]

P_2 Pore pressure at the fracture/matrix interface in the absence of alterations in the reservoir [psi]

P_{clay} Clay pore/osmotic pressure [psi]

P_{Lu} Pore pressure at the end of the water invaded zone [psi]

P_{Ld} Pore pressure at the end of the altered zone [psi]

P_{ob} Overburden pressure [psi]

P_{pore} Pore pressure [psi]

q_g Gas flow rate [Mscf/day]

R Universal gas constant 8.3145 [J/mol K]

$\mathcal{R}$ Membrane efficiency

S_{fD} Fracture skin

S_w Water saturation in the water invaded zone

T   Temperature [K]

$S_{w,CEE}$ Water saturation in the altered zone

$\overline{S_{w,CEE}}$ Average water saturation in the altered zone

S_{wi} Connate water saturation

x_i Length of the altered zone [ft]

x_f Fracture half-length [ft]

x^S Salt concentration [ppm]

$\Delta P_{g,1}$ Ideal pressure drop across the altered zone in the absence of alterations [psi]

$\Delta P_{g,2}$ Additional pressure drop across the altered zone in the presence of alterations [psi]

$\Delta P_{g,d}$ Pressure drop across the altered zone [psi]

$\Delta P_{g,L}$ Pressure drop across Zone 1 [psi]

Greek Letters

α Proportionality constant

β_1 Pore pressure at the end of the altered zone normalized with effective stress at zero permeability

β_2	Clay pore pressure at the end of the altered zone normalized with effective stress at zero permeability
β_3	Overburden pressure normalized with effective stress at zero permeability
β_c	Unit conversion factor, equal to $1.127 * 10^{-3}$
γ_1	Pore pressure gradient normalized with effective stress at zero permeability
γ_2	Clay pore pressure gradient normalized with effective stress at zero permeability
μ_g	Gas viscosity [cP]
π	Osmotic pressure [psi]
ρ_f	Fluid density [Kg/m^3] or [lb/ft^3]
σ'	Normalized effective stress outside the altered zone
σ	Normalized effective stress in the altered zone.
τ_1	Pore pressure at the end of the water invaded zone normalized with effective stress at zero permeability
τ_2	Overburden pressure normalized with effective stress at zero permeability
υ	Salt dissociation coefficient

Subscripts

e	Effective
f	Fluid

g   Gas

c   Constant

w   Water

wi   Irreducible water

 CEE   Capillary end effect

ob   Overburden

TABLE OF CONTENTS

LIST OF FIGURES

LIST OF TABLES

1. INTRODUCTION

Because of the low-porosity and low pore connectivity in resource shales, the oil and gas industry resorted to using hydraulic fracturing as a stimulation technique to produce hydrocarbons at economic rates. While this well stimulation technique provides tremendous advantages for unconventional resource development, careful considerations of the injected water (slick-water) is required to ensure a successful hydraulic fracturing operation. One important consideration is that the injected water is known to interact physically and chemically with shale.

It is widely recognized that the fracturing water invasion creates a region of altered permeability near the fracture/matrix interface. Despite having a limited understanding, it is believed this region plays an important role on the hydrocarbon production rate. The objective of this study is to model the region as a fracture skin explicitly including local physical and chemical phenomena and their associated effects, namely:

(1) permeability improvement due to unpropped fracture development during fracturing

(2) stress increase due to slick water invasion and clay-swelling effect developing after the fracturing, and

(3) water-saturation buildup due to capillary end effect (CEE) developing during the flowback and production.

Permeability improvement due to development of unpropped fractures and cracks near the propped hydraulic fracture is widely accepted by the industry. The resource shales targeted by the companies for oil and gas production are deposited in marine environment. The marine shales are siliceous, holding significant amount of minerals, such as kaolinite, montmorillonite and illite, which make the formation brittle. The brittle rocks have propensity to fracture development and

an operation such as hydraulic fracturing could lead to primary fractures that are propped open and feed directly into the well, and to the secondary fractures and cracks that are unpropped yet still maintain a degree of improvement in delivering the formation fluids to the primary hydraulic fractures. The fractures and cracks develop as the consequence of high-pressure and low-temperature (cold) fracturing water injection. In the literature, the network of primary and secondary hydraulic fractures is often depicted in a dendritic – tree-like – structure. In this conceptualization, following the completion of the fracturing operation, the unpropped secondary fractures are not fully closed and maintain a region of improved permeability near the primary hydraulic fractures. In essence, in their own unique – but limited – way, the secondary fractures contribute to the size of the so-called stimulated reservoir volume (SRV). Some of the commercial reservoir flow simulation and production software used by the unconventional industry allow modeling dual-permeability shale matrix with a far-field low permeability (in the order of 10-100 nano-Darcy) associated with the unaltered matrix, and with near-fracture improved permeability (in the order of 1-10 micro-Darcy) associated with the stimulated zone.

In this work the location of these secondary fractures near the hydraulic fracture/matrix interface is considered as the stimulated zone. I treat this zone in my thesis as the hydraulic fracture skin, not only including the secondary fractures and cracks but also the fracturing water invasion.

The second aspect of the fracture skin modeling involves the fracturing water invasion. Notice that the invasion develops mainly after the fracturing operations. Because the fracturing is a relative rapid process, developing in hours, the injected water does not have sufficient amount of time to penetrate into a tight matrix during the injection operation. However, during the well shut-in, flow back, and production periods, the injected water residing in the hydraulic fracture has ample time to invade into the matrix and interact with shale. This invasion is mainly due to forced
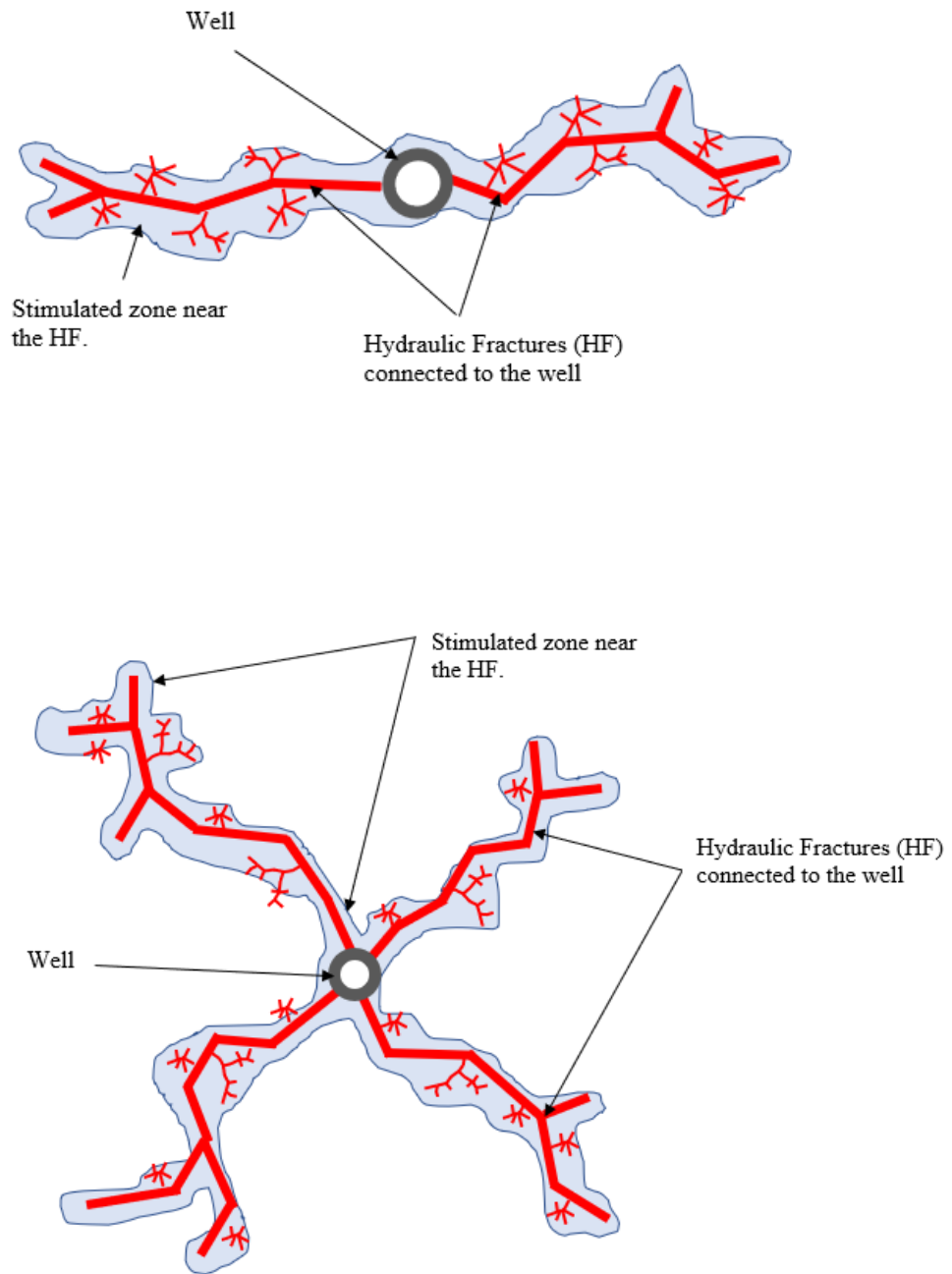
Figure1 – **Complex fracture development with primary propped fractures connected to the well and secondary unpropped fractures with dendritic "tree-like" structure.**

imbibition driven by the fracture pressure fall-off during the shut-in and spontaneous imbibition (water invasion due to capillarity) during the production. Below, I delve into the water invasion and water shale interactions that lead to formation damage during these stages.

1.1.Shut-in Period

First, the formation damage that occurs during the well shut-in period is investigated. Elputranto and Akkutlu (2020) argue that the most paramount physical phenomenon that develops during the well shut-in period is the imbibition of the cold and fresh (low-salinity) water into the formation. During this stage, the cold and fresh water invades into the fractures displacing the gas in the formation and creating a multi-phase flow environment near the fracture. Unfavorable water saturation conditions during the production can influence the gas flow and, consequently, hinder the gas well performance (Eveline et al., 2016). Because the water invaded region and the fractures are relatively colder than the reservoir, local effective stresses instantly decrease, and a conductive heat transfer is triggered from the shale gas reservoir towards the cold water invaded zone leading to the formation of thermally induced micro-fractures near the fracture-matrix interface due to the abrupt changes in local stresses (Eveline et al., 2019). Elputranto and Akkutlu. (2020) argue that these micro-fractures will most likely not contribute to the formation permeability because they are not propped and will therefore close during hydrocarbon production as the pore pressure is reduced. Figure 2 depicts the processes taking place during the shut-in period following a hydraulic fracturing operation.

In addition to imbibition and heat conduction, a molecular diffusion phenomenon known as osmosis develops locally in the water invaded region due to the high clay content of the resource shale matrix. Because some clay minerals act as semi-permeable membrane for diffusion to happen and the invaded water in the pore network has lower temperature and salinity than formation water,
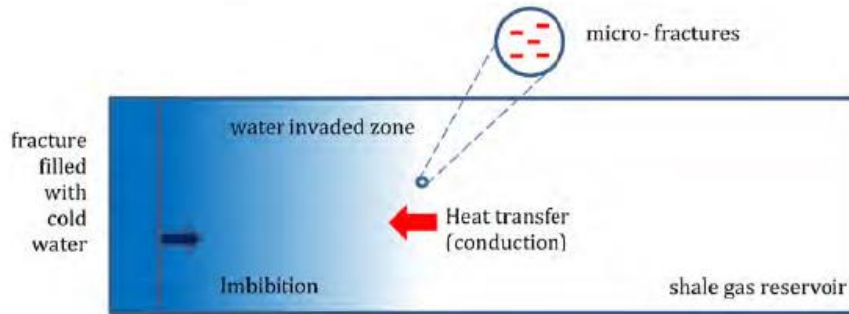
Figure 2. The diagram shows the processes that occur during the well shut-in period following a hydraulic fracturing operation. The blue color represents water saturation in the fracture and the formation. The arrows show the direction of mass/heat transfer (Elputranto and Akkutlu., 2020).

these differences in salinity and temperature between the invaded water and the formation water cause an imbalance in the chemical potential enabling the diffusion of the freshwater molecules into the clay pores. Salt ions can also diffuse in the opposite direction to the pore network, but because the number of ions transferred is limited and mainly controlled by the membrane efficiency of the clays in contact with water, there will be a net mass transfer of ions into the clay pores. A large enough net mass transfer of ions can lead to clay pore pressure build-up or the osmosis pressure to cause clay swelling, a mechanical impact resulting from the re-arrangement of the clay structure (as shown in Figure 3). Eveline et al. (20017) argued that swelling over time could significantly change the local stress field in the matrix near the water invaded zone altering the petrophysical properties (porosity and permeability) of the formation which will lead to the closing of cracks. Consequently, they argued that because the pore network includes mainly cracks and micro-fractures formed in geological time and that these cracks are prone to changing stresses, the main formation damage that occurs during the well's shut-in period is permeability damage.
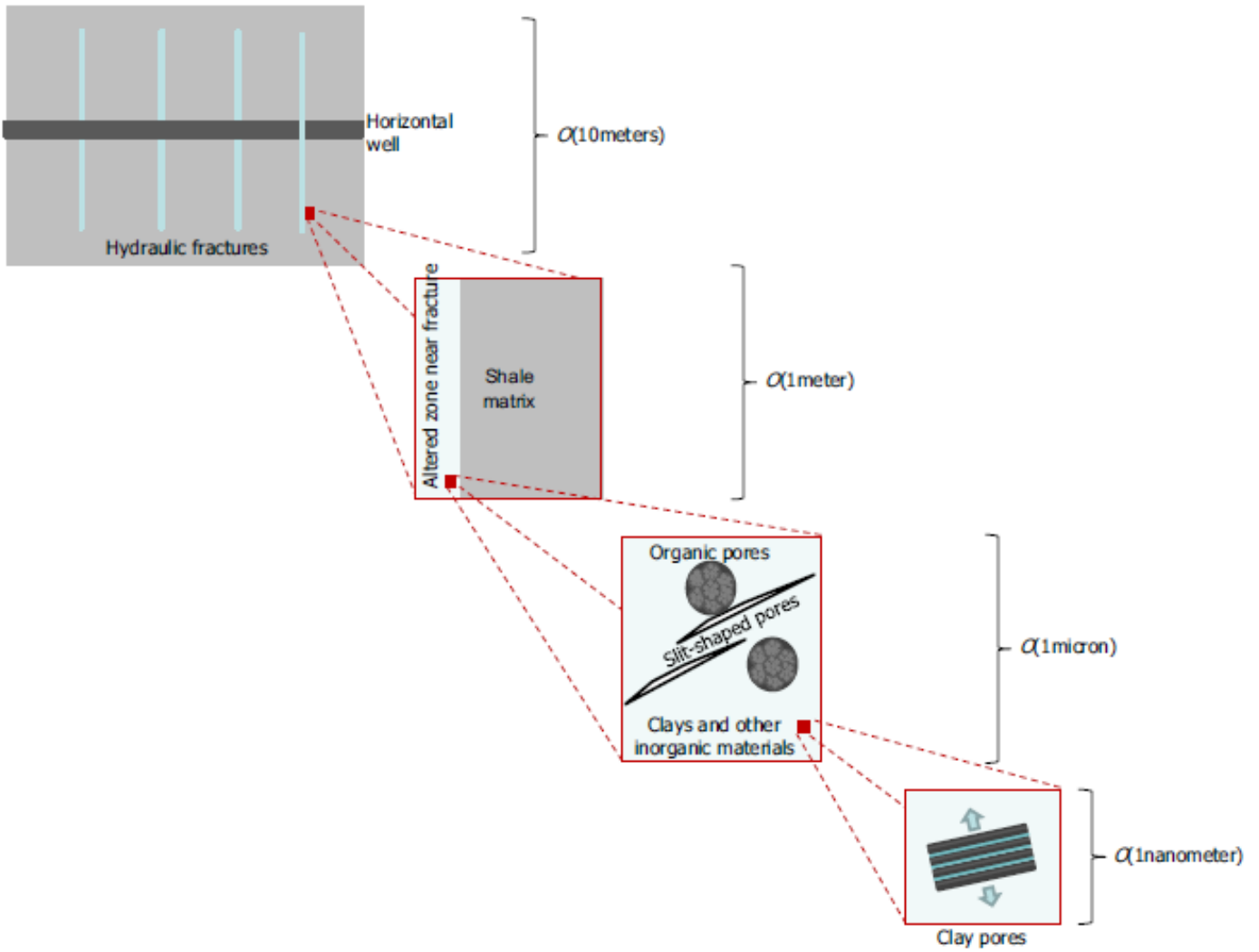
Figure 3. Conceptual petrophysical model of shale matrix with altered zone due to hydraulic fracturing. The blue arrows represent the swelling-related stress caused by water invasion into clay interlayer pores (Eveline et al., 2016).
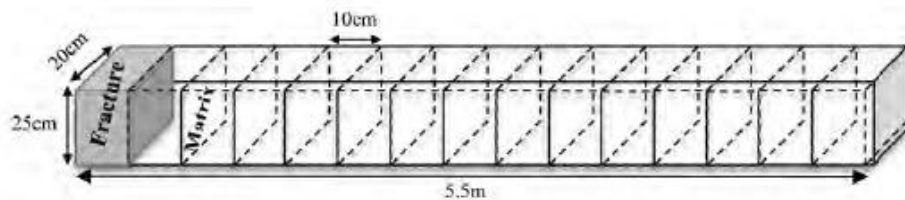
Figure 4. One dimensional simulation model (55 x 1 x 1) representing a hydraulic fracture (on the left) and the shale formation, on the right (Elputranto et al.,2020).

To investigate the impact of temperature imbalance between the fracture and the formation, the effects of osmosis and clay swelling coupled with the temperature imbalance, Elputranto et al. (2019) built a one-dimensional (1D) numerical model to simulate chemo-thermo-poro-elastic system behavior during the shut-in, water flow-back and gas production periods. Further details of their mathematical formulation, development of the numerical models, and model inputs can be found in Elputranto (2020).

Figure 5 shows the variation in temperature with respect to time of the first cell adjacent to the cell containing the fracture (as shown in Figure 4). The black dashed line in Figure 4 represents
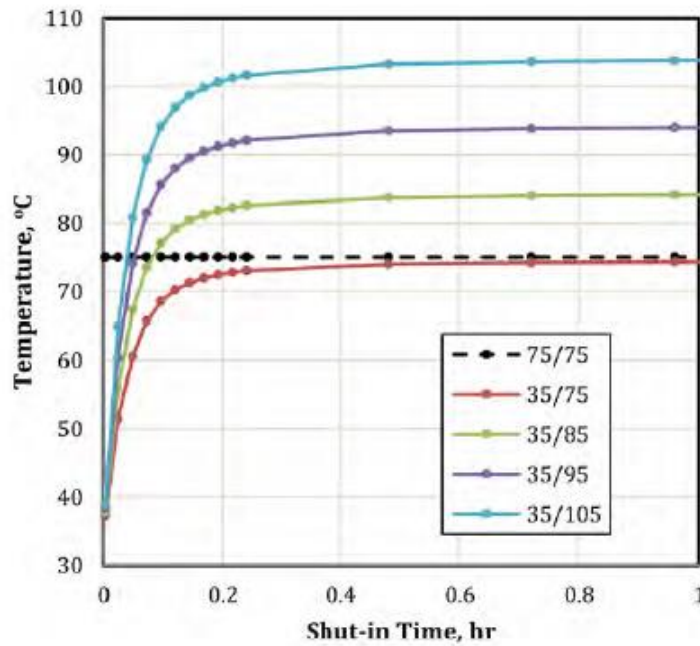
Figure 5. Simulation results of temperature on the first matrix grid block near the fracture during the shut-in period. The black line represents isothermal case, and the color lines represent non-isothermal cases. The legend of 35/75 represents the fracture temperature of 35°C and the formation temperature of 75°C. The system has reached equilibrium at the first fifteen minutes of shut-in period (Elputranto et al.,2020).

the base (reference) case before the injection of the fracturing fluid when temperature is 75℃ everywhere. Regarding the other cases (colored lines), the initial fracture temperature is held at 35℃ while the reservoir temperature is varied between 75-105F. The increase in the initial reservoir temperature can also be considered as a proxy of the increase in formation depth. As shown in Figure 5, temperature equilibrium is reached within the first 15 minutes of shut-in time, which indicates how fast the reservoir heat is conducted to the cold region and heats up the cold fracturing fluid back to the initial reservoir temperature. This happens during the same time scale of imbibition but at a much faster rate than the osmosis and clay swelling phenomena.

Now, the effect of temperature on the capillary pressure and saturation during the shut-in period will be considered. As shown in Figure 6, the increase in reservoir temperature decreases the interfacial tension (between the liquid and gas phase) and, that in turn, reduces the capillary pressure. And because the capillary pressure is reduced, water saturation increases. It is worth noting that the capillary pressure initially decreases at a rapid rate when the temperature imbalance is the largest—that is when the cold fracturing fluid and the rock formation begin to communicate. Following that initial non-linear trend, the capillary pressure decreases at a constant rate at larger shut-in times. The same observation is made when osmosis effect is considered. However, it should be noted that capillary pressure increases to values much higher early during the shut-in when osmosis is considered developing in the water invaded region. Additionally, capillary pressure decline rate is also accentuated in the presence of osmosis. Consequently, water saturation increases significantly with osmosis compared to the case in the absence of osmosis and larger temperature imbalances absorb large water volume. These more pronounced phenomena are due to the clay swelling effect on the shale formation. Elputranto et al. (2020) argue that the increasing capillary pressure effects observed is approximately 10 psi for the cases considered; however, this
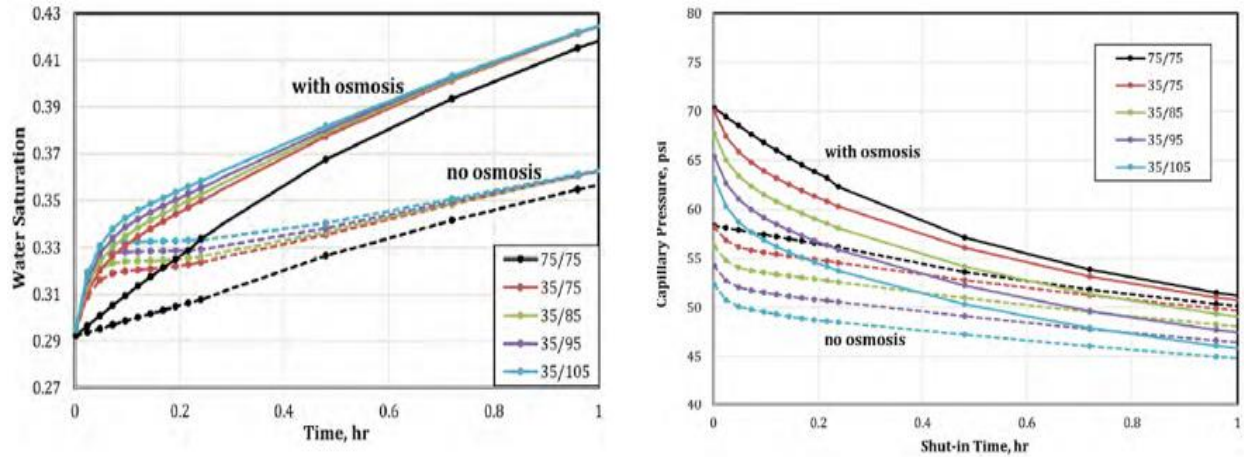
Figure 6. Simulation results of water saturation (left) and capillary pressure (right) versus time on the first matrix grid block near the fracture during the shut-in period. The black dashed lines represent isothermal cases without osmosis and the solid lines represent isothermal cases with osmosis. Clay swelling increases not only the formation capillary pressure but also the decline rate of capillary pressure. Larger temperature imbalance tends to adsorb larger water volume (Elputranto et al.,2020).

value could increase further with the increase in temperature, clay content, and the concentration difference between the fracturing fluid salinity and the clay bound water salinity.

Regarding mean normal stress evolution during the shut-in period, the stress in the cold water invaded region is low, but it increases and approaches to its original value prior to the injection of fracturing water as the invaded region is heated by the reservoir (Figure 7). It should be noted that the trends are nonlinear and become more pronounced when the formation temperature is significantly larger than that of the cold water invaded region. Figure 7 also highlights the associated changes in the stress-sensitive formation permeability during shut-in. The permeability is improved by 5 – 17%. However, as previously noted by Elputranto et al. (2020),

9
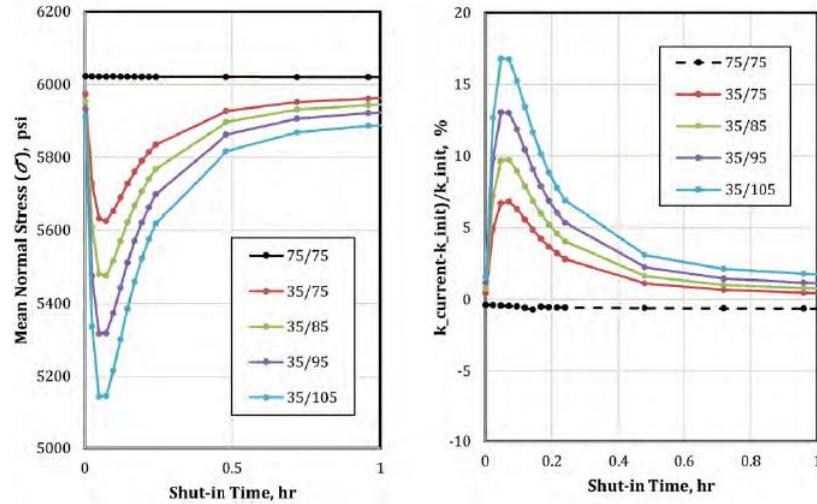
Figure 7. Simulation results of mean normal stress (left) and permeability change (right) versus time on the first matrix grid block during the shut-in period. The black lines represent isothermal cases, and the color lines represent non-isothermal cases. Larger temperature imbalance tends to lower mean normal stress reduction (Elputranto et al.,2020).

the resulting increased permeability due to heat induced micro-fractures will not contribute to the formation permeability because they are not propped and will therefore close.

1.2. Injected Water Flowback and Gas Production Period

Next, the formation damage associated with the flow-back and the production period is discussed (Figure 8). Only a small fraction of the injected water (less than 20 percent) is ultimately recovered from the shale gas wells during the flow-back period. Elputranto and Akkutlu (2018) argues that the difficulty in flowing back the invaded water is not exclusively due to the capillary forces in the water invaded region overcoming the applied pressure forces, but also due to the capillary end effect (CEE) developing near the fracture-matrix interface. This is because in ultralow-permeability formations (resource shales), the sizes of the pores and cracks contributing

10
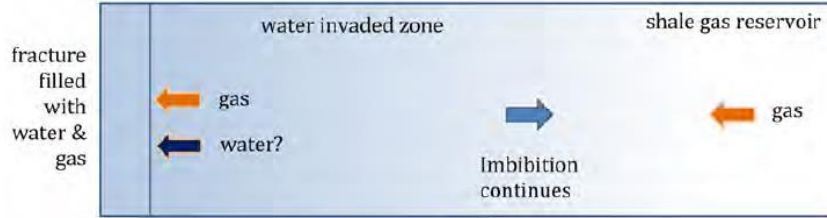
Figure 8. The diagram shows the processes that occur during the water flow-back and gas production periods following a hydraulic fracturing operation. The blue color represents water saturation in the fracture and the formation. The arrows show the direction of mass/heat transfer (Elputranto et al., 2020).

to the transport of fluids are significantly diminished. As such, when fresh fracturing water invades, the formation will experience large gas-water capillary pressure. As a result, the two-phase flow dynamics during the flowback could be controlled by capillary forces. In the presence of strong capillarity in the formation, capillary discontinuity occurs at the fracture/matrix interface, which causes accumulation of water and creates capillary end effect (CEE). Consequently, the distribution of water saturation along the formation becomes nonuniform. CEE retains the injected water within the formation and this water retention could cause high levels of immobile water saturation near the fracture-matrix interface and significantly amplify the liquid blocking in the formation. Furthermore, CEE causes water pressure to be higher during the production period, which affects the well productivity negatively.

To investigate the impact of CEE, the output of the simulation of shut-in period was used as updated input for the water flow back and gas production period. Elputranto et al. (2020) argue that the presence of the Capillary End Effect (CEE) changes the water drainage characteristics of gas in the water invaded zone. It is worth noting that the formation is now under isothermal conditions as the reservoir temperature has risen to its initial value prior to the cold-water injection.

11
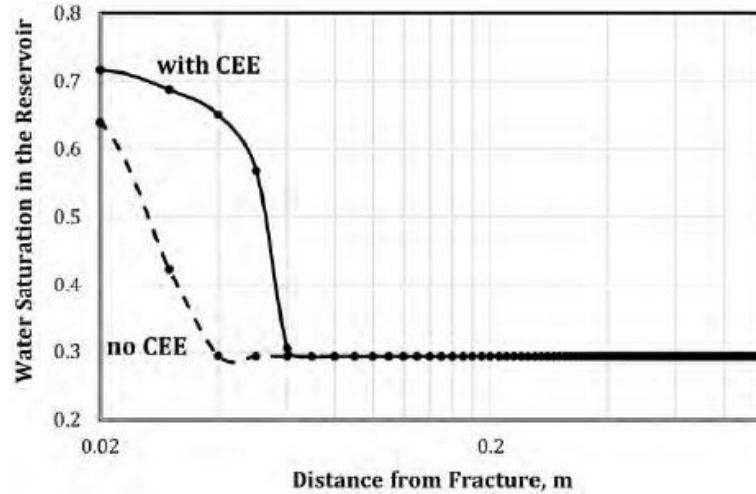
Figure 9. The predicted water saturation profile during 1 day of shut-in and 60 days of production (DP60). The production runs with (solid black line) and without (black dashed line) CEE. CEE increase water saturation in the vicinity of the fracture. The fracture pressure is kept at 2,500 psi during the production to represent a relatively low-pressure drawdown (Elputranto et al., 2020).
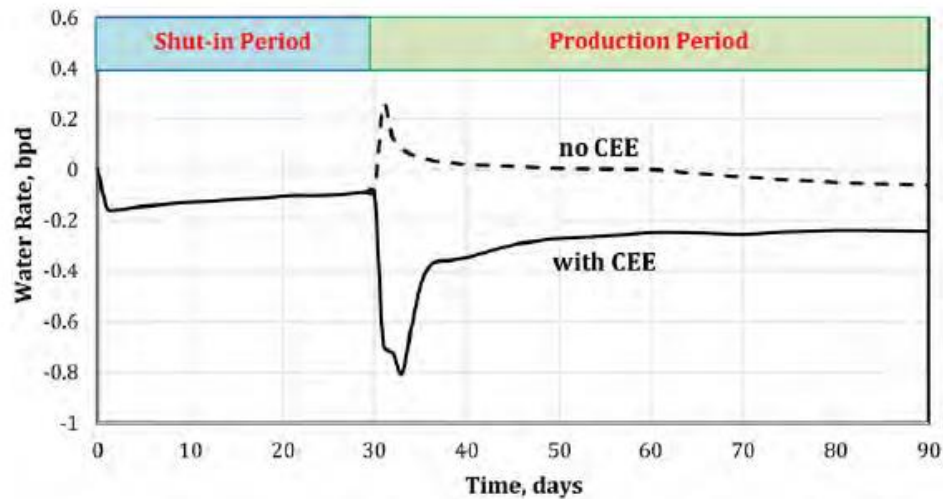
Figure 10. Simulation results of water rate at the second matrix element adjacent to the fracture for 30 days shut-in followed by low-pressure drawdown product. The simulation runs without CEE (dashed line) and with CEE (solid line) (Elputranto et al., 2020).
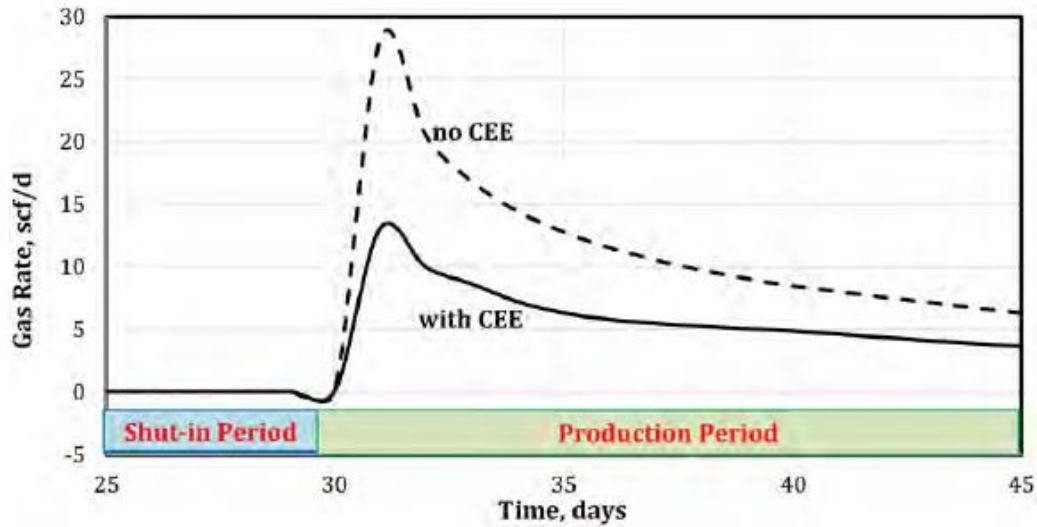
Figure 11. Simulation results of gas rate during low-pressure drawdown production. The simulation runs without CEE (dash line) and with CEE (solid line) (Elputranto et al., 2020).

It was observed that the interstitial water saturation becomes higher closer to the fracture, while gas and water become less mobile. As shown in Figure 9, water saturation increases significantly in the presence of CEE and becomes more pronounced near the fracture.

Additionally, Capillary End Effect causes water pressure to be higher during the production period, which negatively affects the well productivity as previously mentioned. As shown in Figure 10, the first few days of production show a high-water flow rate with the presence of CEE, which then reduces as the pressure between the fracture and the adjacent formation cell becomes uniform and equal to 2500 psi. Elputranto et al. (2020) argue that local capillary forces are dominant at this stage and water invasion due to imbibition continues, hence, the negative water flow rate. When dominant in early production, CEE impact to water rate can only be observed up until 3 cm away from the fracture. Regarding gas production, gas rate is also lower when CEE is included in the simulation model as shown in Figure 11. However, it should be noted that in early days of

13

production period, because of water production, gas saturation increases up to 20 % compared to the residual amount, hence the production of more gas. When water imbibition causes more water invasion to the region later on, local gas saturation decreases.

Next, the impact of pressure drawdown on CEE is discussed. As shown in Figure 11, the impact of CEE is reduced by increasing the pressure drop during the production. Elputranto and Akkutlu (2018) argue that it is because large pressure drop increases the viscous forces in the system, which increases the flow rates. This effect is shown by reducing the fracture pressure from 2500 to 500 psi after 30 days of shut in. The effect of effective stress on permeability near the fracture after the increase in pressure drop is also studied. As shown in Figure 13, the permeability reduction due to stress increases by increasing the pressure drop on production. Consequently, gas rate tends to be higher when effect of stress is not included, especially after the very early stages of production.
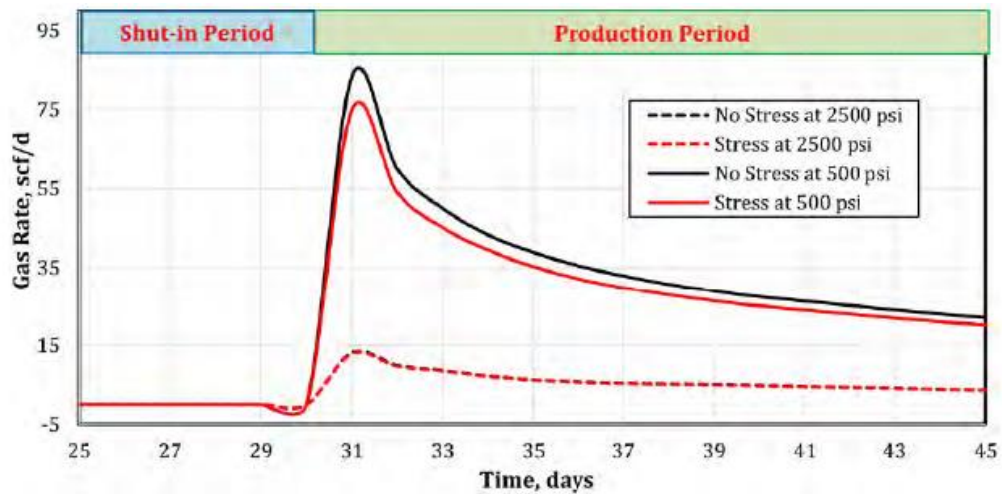
Figure 12. Simulation results of gas rate during low-pressure (dash line) and high-pressure (solid line) drawdown production. Less water wet rock is used for the simulations. The micro-fracture permeability is considered constant in black lines and stress-depend in red lines. (Elputranto et al., 2020).
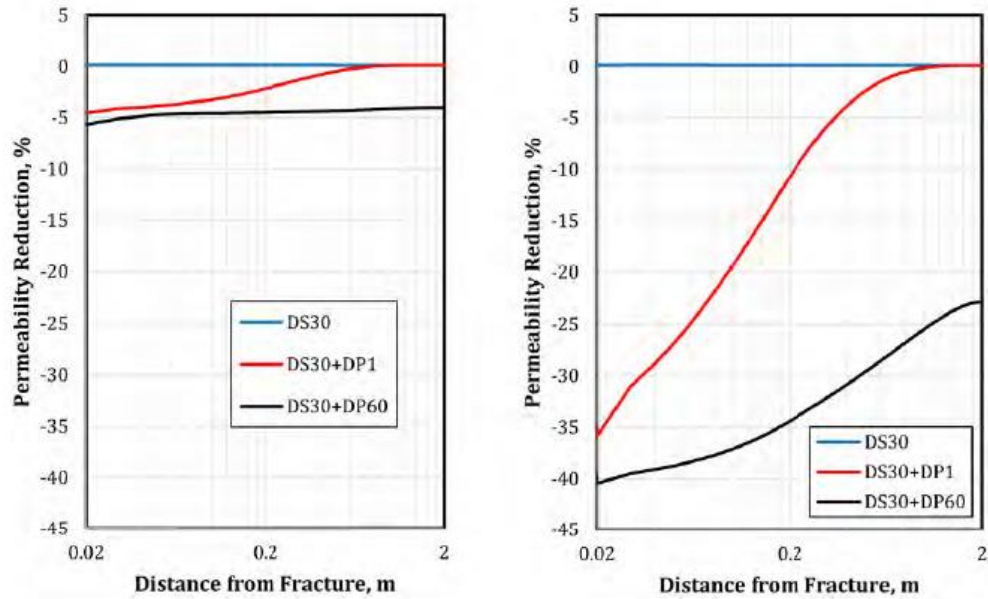
Figure 13. Simulation results with dynamic permeability due to stress during low-pressure drawdown production (left). The simulation runs for 30 days of the shut-in (blue) and continued by 1 (red) and 60 (black) days of production. The permeability reduction due to stress increases by increasing the pressure drop on production. Simulation results with dynamic permeability due to stress during high-pressure drawdown production. The simulation runs for 30 days of the shut-in (blue) and continued by 1 (red) and 60 (black) days of production. The permeability reduction due to stress increases by increasing the pressure drop on production (Elputranto et al., 2020).

Finally, the effect of non-uniform stress field will be considered in the discussion of the damage during the production period. As previously discussed, changes that occur due to non-uniform stress field to water saturation, permeability and mean normal stress can affect the well's performance during both flowback and gas production. For this study, two cases are considered: Base Case and Case 1. The Base Case is the case where the impact of temperature and osmotic pressure observed during the first few minutes of shut-in disappear in time; however, the changes
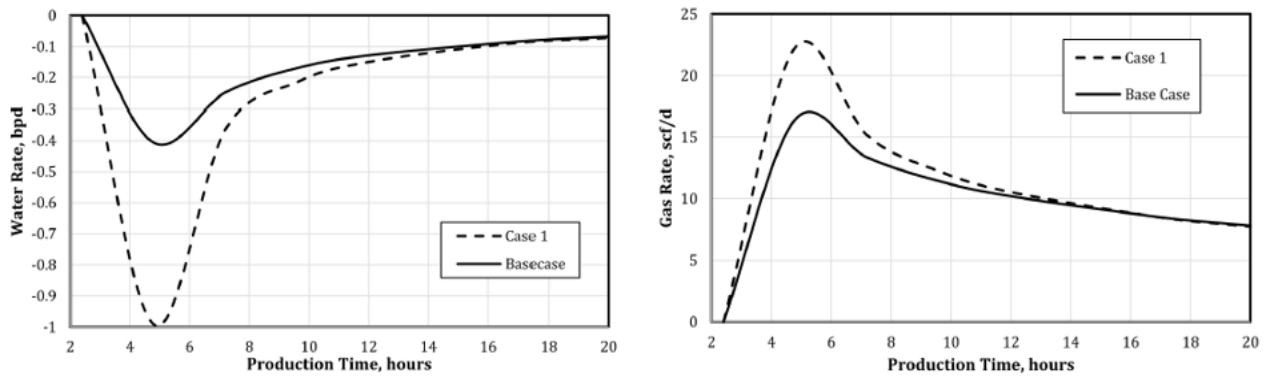
Figure 14. Simulation results of water rate in the first matrix grid block during production (left). Higher water absorption during shut-in time because of non-uniform stress fields tend to increase the water blocking caused by CEE. Simulation results of gas rate during low-pressure drawdown production (right). Non-uniform stress field boosts gas rate at early time of production (Elputranto et al., 2020).

in the mean normal stress (hence, permeability) fields and phases saturations prevail over time. Further detail of the input values for the Base Case can be found in Elputranto et al. (2020).

Regarding Case 1, this case includes the non-uniform field considerations. Furthermore, formation temperature is 105℃ and injected freshwater temperature is 35℃. The flow-back and production is simulated considering non-uniform fields as the initial conditions. The simulation is run with the presence of CEE by maintaining a constant pressure of 2500 psi in the fracture element for 72 hours. Thermal effect and osmosis effect during shut-in are also included in the simulation run of Case 1. As shown in Figure 14, water rate is significantly higher in Case 1, where non-uniform stress fields effect water blocking due to CEE. Gas rate is also observed to be higher than the Base Case in early stages of production, especially shortly after shut-in period.

16

2. METHODOLOGY

To model fracture skin, we consider two cases: In Case 1, gas flow occurs in the absence of alterations in the formation, whereas Case 2 considers gas flow occurs in a region in the presence of the mentioned alterations. The difference in the derived pressure drops between the two cases (i.e., Case 2 minus Case 1) is the pressure drop due to the three combined effects.

2.1. Case 1 – Gas Flow Without Any Alterations

For Case 1, the following assumptions are made:

1. There is a steady-state single-phase gas flow in the uninvaded reservoir region.

2. There is a steady-state two-phase (gas and water) flow in the invaded region.

3. Water saturation is constant throughout each zone and there is a step-like water saturation between zones.

4. The invaded fluid (slick water) moves at such a low rate that its depth into the formation can be assumed to be constant (L = constant).
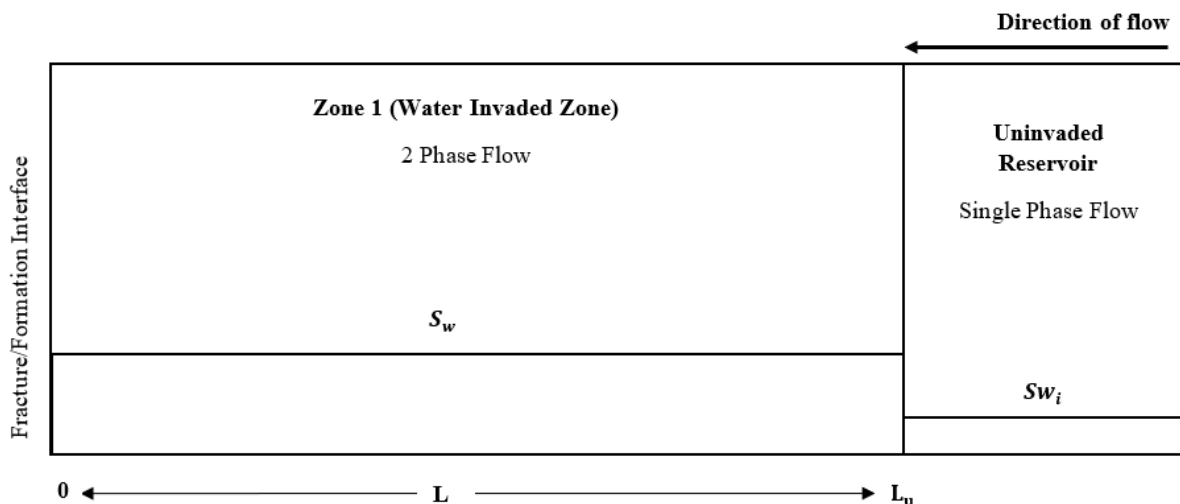
Figure 15. Schematic of water saturation through each reservoir region in the absence of alterations in the formation matrix.

17
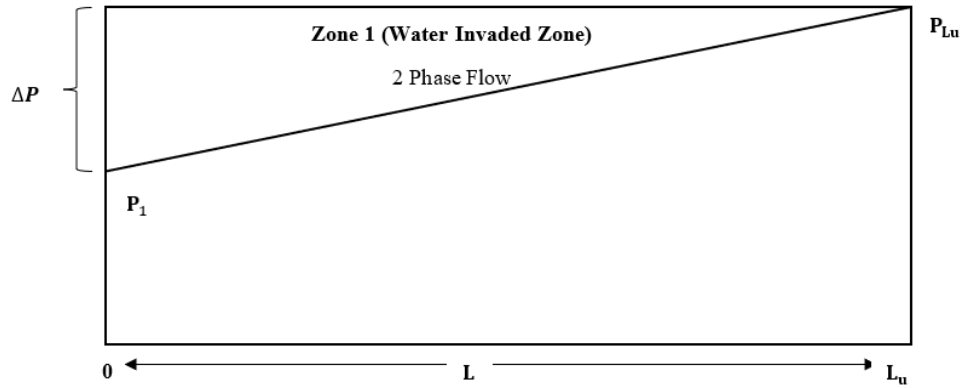
Figure 16. Schematic of the considered pressure drop across the water invaded region.

Figure 15 and 16 show water saturation through each reservoir region in the absence of alterations to the formation matrix and the considered pressure drop across the water invaded region, respectively. In the absence of any alterations, fluid follow during production or flowback obeys Darcy's Law and is given by:

$$q_g = \frac{\beta_c A_e k_{rg} K}{\mu_g} \qquad\qquad 1$$

where k_{rg} and K are gas relative permeability and stress-sensitive formation permeability, respectively. β_c is the unit conversion factor $(1.127 * 10^{-3})$ for the practical oilfield units while μ_g is the gas viscosity. Lastly, A_e is the fracture effective cross-sectional area and is given by:

$$A = 2\, x_f h \qquad\qquad 2$$

$$A_e = A\,(1 - S_w) \qquad\qquad 3$$

Substituting for the effective fracture cross-sectional area and rearranging to solve for pressure, the equation becomes:

$$\int_{P_1}^{P_{Lu}} dP_g = \frac{q_g\, \mu_g}{2\,\beta_c\, x_f h\,(1-S_w)k_{rg}} \int_0^{L_u} \frac{1}{K}\,dx \qquad\qquad 4$$

Because resource shales consist of micro-cracks and fractures, which can provide major connectivity at low effective stress conditions, Gangi's (1978) stress sensitive permeability equation is substituted into equation 4:

$$K = K_0 \left[1 - \left(\frac{P_{ob} - \alpha P_{pore}}{P_0} \right)^m \right]^3 \qquad 5$$

where K_0 is the formation permeability at zero effective stress, P_{ob} is the overburden or confining pressure, P_{pore} is the pore pressure, P_0 is the effective stress at zero permeability and m is the strength of the pore to hold the aperture open. Equation 4 then becomes as follows:

$$\Delta P = \frac{q_g \, \mu_g}{2 \, \beta_c \, x_f h \, (1-S_w) k_{rg} K_0} \int_0^{L_u} \frac{1}{\left[1 - \left(\frac{P_{ob} - \alpha P_{pore}}{P_0} \right)^m \right]^3} dx \qquad 6$$

Assuming that αP_{pore} is a linear function of distance (x) and the overburden pressure (P_{ob}) is constant:

$$\sigma(x)' = \frac{P_{ob}}{P_0} - \frac{\alpha P_{pore}}{P_0} \qquad 7$$

$$\frac{\alpha P_{pore}}{P_0} = ax + \tau_1 \qquad 8$$

$$\frac{P_{ob}}{P_0} = \tau_2 \qquad 9$$

The normalized pore pressure will have a positive slope because pore pressure decreases as fluid approaches the fracture/matrix interface (x = 0). Then, the effective stress function normalized with stress at zero permeability (stress required to close a fracture) becomes:

$$\sigma(x)' = \tau_2 - (ax + \tau_1) \qquad 10$$

$$\sigma(x)' = -ax + (\tau_2 - \tau_1) \qquad 11$$
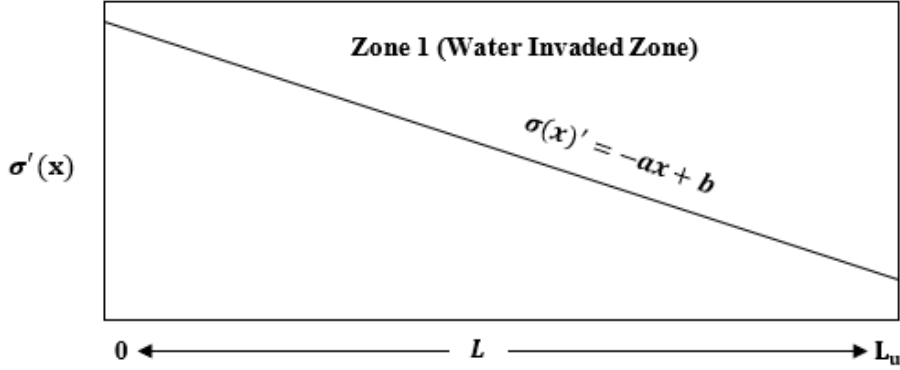
Figure 17. Schematic of the normalized effective stress as a function of length across the water invaded region.

$$\sigma(x)' = -ax + b \qquad\qquad 12$$

where *a* and *b* are the gradient of the normalized effective stress and the normalized effective stress at the matrix/fracture interface in the absence of alterations in the formation matrix, respectively.

As shown in Figure 17, the normalized stress function will be increasing with decreasing distance away from the fracture/matrix interface as a result of decreasing pore pressure with distance.

Substituting $\sigma(x)'$ into the pressure drop equation, the equation then becomes:

$$\Delta P = \frac{q_g\,\mu_g}{2\,\beta_c\,x_f h\,(1-S_w)k_{rg}K_0} \int_0^{L_u} \frac{1}{[1-(b-ax)^m]^3}\,dx \qquad\qquad 13$$

Next, alterations due to the three combined effects will be considered, namely: high-permeability due to unpropped fracture development during fracturing, high-stress due to slick water invasion and clay-swelling effect (CEE) developing after the fracturing, and high water-saturation due to capillary end effect developing during the flowback and production.

2.2.Case 2 – Gas Flow in the Presence of Alterations

For Case 2, the following assumptions are made:

1. Improved permeability, clay swelling, and CEE all develop in zone 2.

2. There is a steady-state single-phase gas flow in the uninvaded zone.

3. There is a steady-state two-phase flow (gas and water) in the invaded regions (zone 1 and 2)

4. Water saturation is constant throughout each zone and there is a step-like water saturation between zones.

5. The invaded fluid moves at such a low rate that its depth into the formation can be assumed to be constant (L = constant)

Figure 18 and 19 show water saturation through each reservoir region when alterations occur and the considered pressure drop across the water invaded region, respectively. To formulate the equation of the pressure-drop across the water invaded region, the pressure-drop across the region where no formation alterations take place (Zone 1) is derived, and then the pressure drop
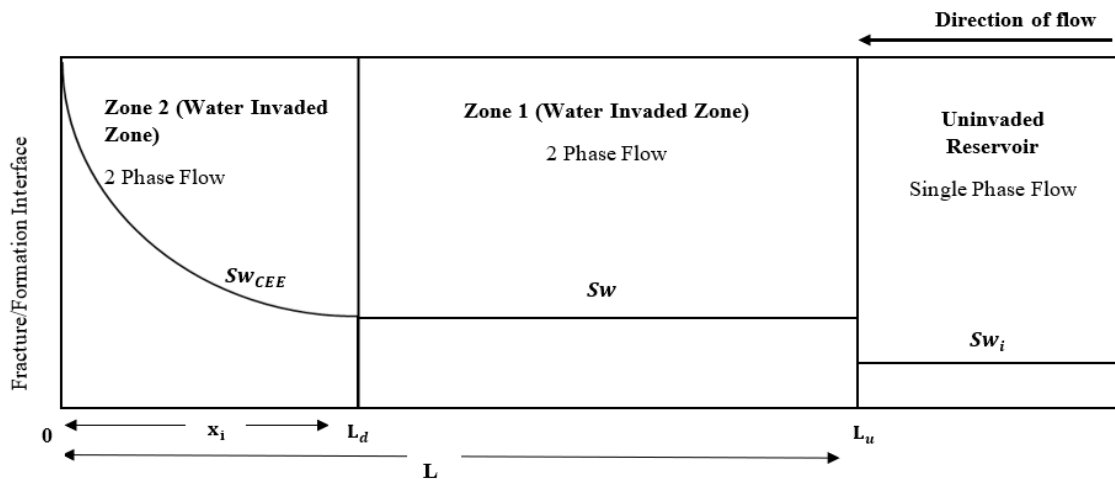
Figure 18. Schematic of water saturation through each reservoir region for when alterations occur.
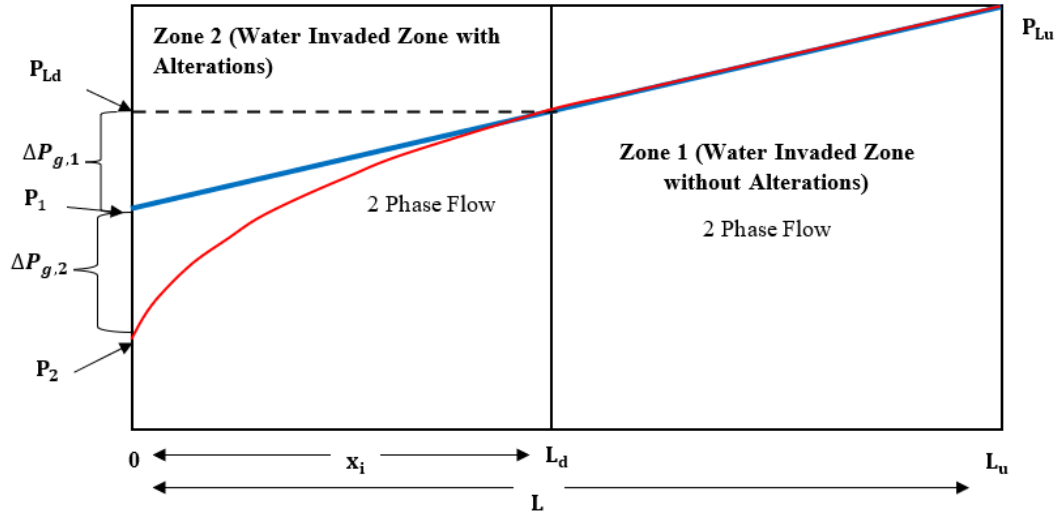
Figure 19. Schematic of the considered pressure drop across the water invaded regions. The red line represents the pressure drop across the water invaded zones when alterations develop in Zone 2. The blue line represents the pressure in the absence of alterations/damage.

across the region where formation alterations develop (Zone 2) is derived. The sum of the two pressure drops is the total pressure drop across the entire water invaded region.

2.2.1. Gas Flow Through Zone 1 (Water Invaded Zone)

In Zone 1 where there is slick water invasion into the formation matrix but no matrix alterations, gas flow during production obeys Darcy's Law and is given by:

$$q_g = \frac{2\,\beta_c\,x_f h\,(1-S_w)k_{rg}K}{\mu_g}\frac{dP_g}{dx} \qquad\qquad 14$$

Solving for the pressure and substituting for Gangi's (1978) stress sensitive permeability equation, the pressure drop equation becomes:

$$P_{Lu} - P_{Ld} = \frac{q_g \, \mu_g}{2 \, \beta_c \, x_f h \, (1-S_w) k_{rg}} \int_{L_d}^{L_u} \frac{1}{K_0 \left[1-\left(\frac{P_{ob}-\alpha P_{pore}}{P_1}\right)^m\right]^3} \, dx \qquad 15$$

Substituting for the effective stress function normalized with stress at zero permeability derived in the previous section (equation 12), equation 15 becomes:

$$\Delta P_{g,L} = \frac{q_g \, \mu_g}{2 \, \beta_c \, x_f h \, (1-S_w) k_{rg} K_0} \int_{L_d}^{L_u} \frac{1}{[1-(b-ax)^m]^3} \, dx \qquad 16$$

2.2.2. Gas Flow Through Zone 2

In Zone 2, slick water invades the formation matrix and causes formation alterations due to the three effects previously described. To account for damage due to capillary-end-effect (CEE), a new associated gas relative permeability defined as $k_{rg,CEE}$ is introduced. Permeability improvement due to unpropped fracture development during fracturing is accounted for by introducing a stress sensitive permeability (K_{clay}) while damage due to clay swelling is introduced by adding an osmotic pressure term into the stress sensitive permeability model. Thus, gas flow across zone 2 is given by:

$$q_g = \frac{\beta_c A_e k_{rg,CEE} \, K_{clay}}{\mu_g} \frac{dP_g}{dx} \qquad 17$$

$k_{rg,CEE}$ and K_{clay} are gas relative permeability and stress-sensitive formation permeability in the altered zone, respectively. β_c is the unit conversion factor ($1.127 * 10^{-3}$) while μ_g is the gas viscosity. A_{CEE} is the fracture effective cross-sectional area and is given by:

$$A_{CEE} = A \, (1 - S_{w,CEE}) \qquad 18$$

Substituting for the effective fracture cross-sectional area and rearranging to solve for pressure, the equation becomes:

$$dP_g = \frac{q_g\,\mu_g}{2\,\beta_c\,x_f h\,(1-S_{w,CEE})k_{rg,CEE}\,K_s}\,d_x \qquad\qquad 19$$

The stress sensitive permeability is defined as follows:

$$K_{clay} = K_s\left[1 - \left(\frac{P_{ob}-\alpha P_{pore}+P_{clay}}{P_1}\right)^m\right]^3 \qquad\qquad 20$$

where P_{clay} is the osmotic pressure which acts net compressive stress leading to clay swelling and

K_s is the improved permeability due to unpropped fractures and cracks.

In the altered zone (zone 2), water saturation ($S_{w,CEE}$) is a function of distance. Consequently, the gas relative permeability in this zone ($k_{rg,CEE}$) will also be a function of distance. To resolve the distance dependency, constant average water saturation is considered, which in turn, results in a constant average gas relative permeability given by the following expression, respectively: $\overline{S_{w,CEE}} = \frac{S_{w,CEE}}{x_i}$ and $\overline{k_{rg,CEE}} = k_{rg,CEE}(\overline{S_{w,CEE}})$.

Substituting for $\overline{S_{w,CEE}}$, $\overline{k_{rg,CEE}}$, and K_{clay} and integrating for the pressure drop, equation 19 becomes:

$$\Delta P_{g,d} = \frac{q_g\,\mu_g}{2\,\beta_c\,x_f h\,(1-\overline{S_{w,CEE}})\overline{k_{rg,CEE}}\,K_0}\int_0^{L_d}\frac{1}{\left[1-\left(\frac{P_{ob}-\alpha P_{pore}+P_{clay}}{P_0}\right)^m\right]^3}\,dx \qquad\qquad 21$$

Next, αP_{pore} and P_{clay} are assumed to be linear functions of distance (x) and the overburden pressure (P_{ob}) is constant:

$$\frac{\alpha P_{pore}}{P_0} = \gamma_1\,x + \beta_1 \qquad\qquad 22$$

$$\frac{P_{clay}}{P_0} = -\gamma_2\,x + \beta_2 \qquad\qquad 23$$

$$\frac{P_{ob}}{P_0} = \beta_3 \qquad\qquad 24$$

The normalized pore pressure and clay pore (osmotic) pressure have positive and negative slopes, respectively. This is because as fluid (gas) approaches the fracture/matrix interface, pore pressure decreases while osmotic pressure increases as water tends to accumulate near the interface due to the capillary-end-effect. The effective stress is then defined as follows:

$$\sigma(x) = \frac{P_{ob}}{P_0} - \frac{\alpha P_{pore}}{P_0} + \frac{P_{clay}}{P_0} \qquad\qquad 25$$

$$\sigma(x) = \beta_3 - (\gamma_1 x + \beta_1) + (-\gamma_2 x + \beta_2) \qquad\qquad 26$$

$$\sigma(x) = (\beta_3 - \beta_1 + \beta_2) - (\gamma_2 + \gamma_1)x \qquad\qquad 27$$

$$\sigma(x) = d - cx \qquad\qquad 28$$

where c and d are the gradient of the normalized effective stress and the normalized effective stress at the matrix/fracture interface in the presence of alterations, respectively, when alterations occur in zone 2.

Substituting for the effective stress, $\sigma(x)$, into the pressure drop equation, equation 21 becomes:

$$\Delta P_{g,d} = \frac{q_g \, \mu_g}{2 \, \beta_c \, x_f h \, (1 - S_{w,CEE}) \overline{k}_{rg,CEE} \, K_s} \int_0^{L_d} \frac{1}{[1 - (d - cx)^m]^3} dx \qquad\qquad 29$$

Adding up the pressure drop terms across zone 1 and zone 2, the resulting total pressure drop is given by:

$$\Delta P_{total} = \Delta P_{g,L} + \Delta P_{g,d} \qquad\qquad 30$$

$$\Delta P_{total} = \frac{q_g\,\mu_g}{2\,\beta_c\,x_f h\,K_0}\left[\frac{1}{(1-S_w)k_{rg}}\int_{L_d}^{L_u}\frac{1}{[1-(b-ax)^m]^3}dx\; +\right.$$

$$\left.\frac{1}{(1-\overline{S_{w,CEE}})\overline{k}_{rg,CEE}}\frac{K_0}{K_s}\int_0^{L_d}\frac{1}{[1-(d-cx)^m]^3}dx\right]\tag{31}$$

2.2.3. Skin Effect

As previously mentioned, the difference in the derived pressure drops between the two

cases (i.e., Case 2 minus Case 1) is the pressure drop due to the three combined effects.

$$\Delta P_s = \Delta P_{total} - \Delta P\tag{32}$$

$$\Delta P_s = \frac{q_g\,\mu_g}{2\,\beta_c\,x_f h\,K_0}\left[\frac{1}{(1-S_w)k_{rg}}\int_{L_d}^{L_u}\frac{1}{[1-(b-ax)^m]^3}dx + \frac{1}{(1-\overline{S_{w,CEE}})\overline{k}_{rg,CEE}}\frac{K_0}{K_s}\int_0^{L_d}\frac{1}{[1-(d-cx)^m]^3}dx\; -\right.$$

$$\left.\frac{1}{(1-S_w)K_{rg}}\int_0^{L_u}\frac{1}{[1-(b-ax)^m]^3}dx\right]\tag{33}$$

Factoring for $(1-S_w)K_{rg}$ and $\left(1-\overline{S_{w,CEE}}\right)$, equation 33 becomes:

$$\Delta P_s = \frac{q_g\,\mu_g}{2\,\beta_c\,h\,K_0 k_{rg}}\frac{1}{x_f\,(1-S_w)\left(1-\overline{S_{w,CEE}}\right)}\left[\left(1-\overline{S_{w,CEE}}\right)\int_{L_d}^{L_u}\frac{1}{[1-(b-ax)^m]^3}dx\; +\right.$$

$$\left.\frac{(1-S_w)k_{rg}}{\overline{k}_{rg,CEE}}\frac{K_0}{K_s}\int_0^{L_d}\frac{1}{[1-(d-cx)^m]^3}dx - \left(1-\overline{S_{w,CEE}}\right)\int_0^{L_u}\frac{1}{[1-(b-ax)^m]^3}dx\right]\tag{34}$$

The hydraulic fracture skin is then defined as:

$$\Delta P_s = \frac{q_g\,\mu_g}{2\,\beta_c\,h\,K_0 k_{rg}}S_{fD}\tag{35}$$

$$S_{fD} = \frac{1}{x_f\,(1-S_w)\left(1-\overline{S_{w,CEE}}\right)}\left[\frac{(1-S_w)k_{rg}}{\overline{k}_{rg,CEE}}\frac{K_0}{K_s}\int_0^{L_d}\frac{1}{[1-(d-cx)^m]^3}dx + \left(1-\right.\right.$$

$$\left.\left.\overline{S_{w,CEE}}\right)\int_{L_d}^{L_u}\frac{1}{[1-(b-ax)^m]^3}dx - \left(1-\overline{S_{w,CEE}}\right)\int_0^{L_u}\frac{1}{[1-(b-ax)^m]^3}dx\right]\tag{36}$$

Let $I_1 = \int_0^{L_d}\frac{1}{[1-(d-cx)^m]^3}dx$, $I_2 = \int_{L_d}^{L_u}\frac{1}{[1-(b-ax)^m]^3}dx$, and $I_3 = \int_0^{L_u}\frac{1}{[1-(b-ax)^m]^3}dx$

Using u substitution and the geometric series expansion of $\frac{1}{[1-(d-cx)^m]^3}$, I_1 becomes:

$$I_1 = \sum_{n=2}^{\infty} \frac{(n-1)\,n}{2} \int_0^{Ld} (d - cx)^{m(n-2)}\, dx \qquad\qquad 37$$

Integrating with respect to x and substituting x_i for L_d, I_1 becomes:

$$I_1 = -\frac{1}{2m\,c} \sum_{n=2}^{\infty} \frac{(n-1)\,n}{n+\frac{1}{m}-2} \left[(d - x_i c)^{n*m-2m+1} - d^{n*m-2m+1}\right] \qquad\qquad 38$$

Similarly, I_2 and I_3 are given by:

$$I_2 = -\frac{1}{2m\,a} \sum_{n=2}^{\infty} \frac{(n-1)\,n}{n+\frac{1}{m}-2} \left[(b - L_u a)^{n*m-2m+1} - (b - x_i a)^{n*m-2m+1}\right] \qquad\qquad 39$$

$$I_3 = -\frac{1}{2m\,a} \sum_{n=2}^{\infty} \frac{(n-1)\,n}{n+\frac{1}{m}-2} \left[(b - L_u a)^{n*m-2m+1} - b^{n*m-2m+1}\right] \qquad\qquad 40$$

After plugging I_1, I_2, and I_3 into the fracture skin equation (S_{fD}) and further algebraic manipulation, the fracture skin equation becomes:

$$S_{fD} = \frac{1}{2\ m\ x_f\ (1-S_w)(1-\overline{S_{w,CEE}})} \left[(1 - \overline{S_{w,CEE}}) \sum_{n=2}^{\infty} \frac{(n-1)\,n}{a\left(n+\frac{1}{m}-2\right)} \left[(b - x_i a)^{n*m-2m+1} - \right. \right.$$

$$\left. \left. b^{n*m-2m+1}\right] - \frac{(1-S_w)K_{rg}}{\overline{k_{rg,CEE}}} \frac{K_0}{K_s} \sum_{n=2}^{\infty} \frac{(n-1)\,n}{c\left(n+\frac{1}{m}-2\right)} \left[(d - x_i c)^{n*m-2m+1} - d^{n*m-2m+1}\right] \right] \qquad\qquad 41$$

Because the stress-sensitive rock permeability has been integrated with respect to the length of the altered zone, the equation presented above is for the cumulative skin across the damaged zone. To evaluate the effect of the fracture skin as a function of distance away from the fracture/matrix interface, the skin equation (S_{fD}) is differentiated with respect to the length of the altered zone (x_i). The derivative of S_{fD} is then given by:

$$\frac{\partial S_{fD}}{\partial x_i} = \frac{1}{2\,a\,m\,x_f\,(1-S_w)\left(1-\overline{S_{w,CEE}}\right)}\left[\frac{a}{c}\,\frac{(1-S_w)k_{rg}}{k_{rg,CEE}}\,\frac{K_0}{K_s}\sum_{n=2}^{\infty}\frac{(n-1)\,n}{n+\frac{1}{m}-2}[c*(n*m-2m+\right.$$

$$\left.1)\,(d-x_ic)^{n*m-2m}]-\left(1-\overline{S_{w,CEE}}\right)\sum_{n=2}^{\infty}\frac{(n-1)\,n}{n+\frac{1}{m}-2}[a*(n*m-2m+1)\,(b-x_ia)^{n*m-2m}]\right] \qquad 42$$

3. RESULTS AND DISCUSSION

3.1. Sensitivity Analysis of Damage Skin

To determine the key mechanisms controlling flow during the flow-back of the injected fracturing water and gas production, a scenario, where there is no improvement in permeability due to unpropped fracture development, is considered first (i.e., $K_0 = K_s$). The data shown in Table 1 is used to simulate the fracture skin. As shown in Figure 20, the cumulative fracture skin (S_{fD}) increases with increasing length of the damage zone (zone 2) whereas the gradient of the fracture skin decreases with increasing distance away from the fracture/matrix interface. This decrease in the skin gradient indicates the reduction in the formation damage deeper into the reservoir, which mirrors the accumulation of water near the fracture/matrix interface. With the invasion of the hydraulic fracturing water into the reservoir, the proposed fracture skin model captures the damage mechanisms induced by the transport of the hydraulic fracturing fluid into the rock formation and the interaction of the water with the matrix.

A sensitivity analysis is performed using one-parameter-at-a time approach, each parameter value is changed ±10 percent, while holding the rest of the parameter values constant to gain an improved understanding of the controlling mechanisms.

Table 1. **Parameters used to investigate fracture skin. The values of the parameters obtained from Elputranto and Akkutlu (2018), Elputranto et al. (2020)**

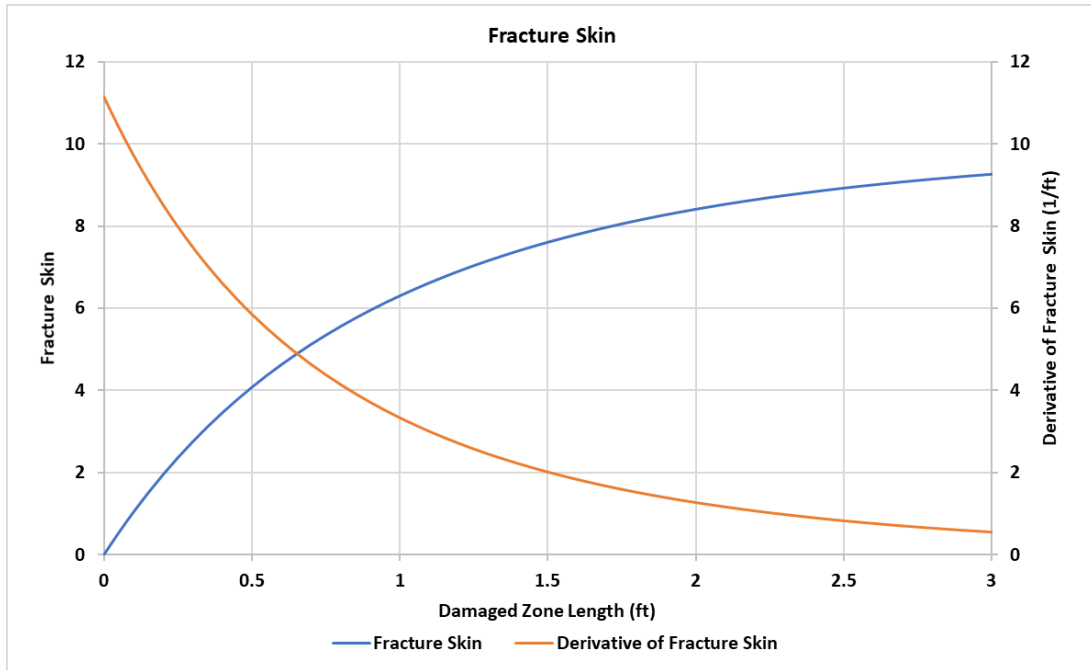| a (1/ft)	b	c (1/ft)	d	m	x_i (ft)	x_f (ft)	k_{rg}	$\overline{k_{rg,CEE}}$	S_w	$\overline{S_{w,CEE}}$	K_0 (md)	K_s (md)
0.1	0.6	0.12	0.7	0.5	4.5	100	0.32	0.16	0.55	0.65	0.00022	0.00022

Figure 20. Plot of fracture skin as a function of the length of the damaged zone. The figure shows fracture skin increasing with increasing distance.
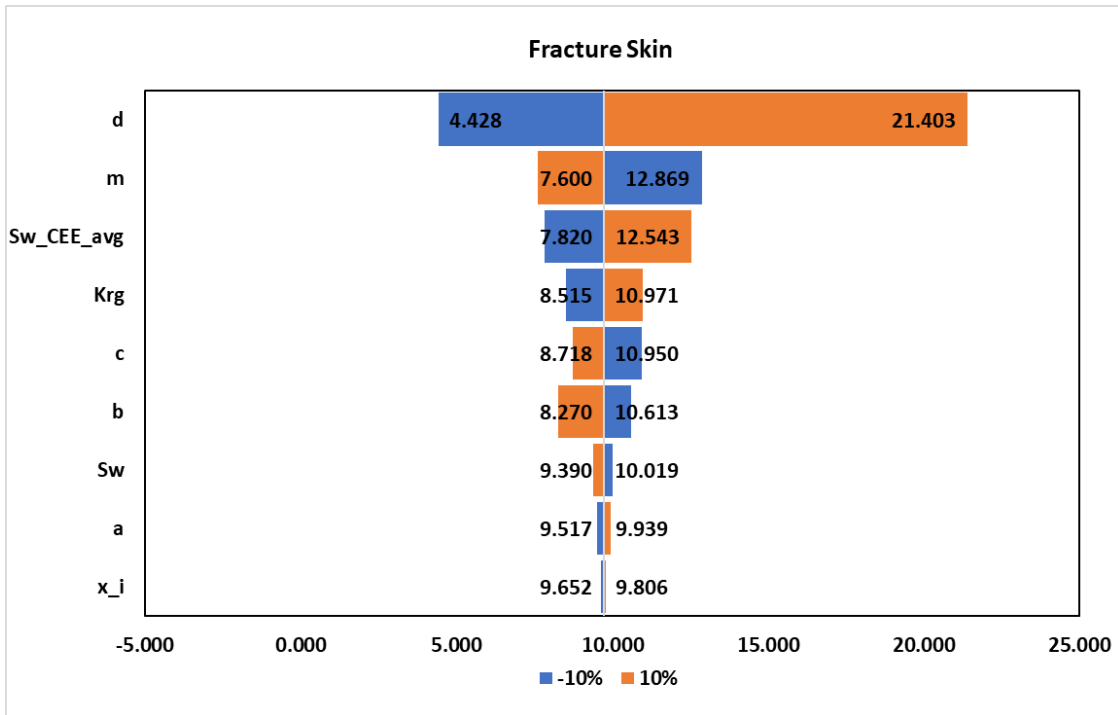

Figure 21. Tornado chart of the parameters in the fracture skin model for formation damage case.

As shown in Figure 21, the result indicates that fracture skin is sensitive to the following parameters in that order: (1) the normalized effective stress at the fracture matrix/interface when clay swelling develops in the altered/damaged zone (d), (2) the strength of the unpropped fractures and cracks to hold the aperture open (m), i.e., their resistance to close, and (3) the average water saturation in the damaged zone ($\overline{S_{w,CEE}}$). Thus, it can be concluded that clay swelling is the predominant damage mechanism as the two most sensitive parameters (d and m) are geo-mechanical parameters of the stress-sensitive permeability model, which are primarily impacted by clay swelling. On the other hand, the contribution of the capillary end effect to the fracture skin is mainly controlled by the average water saturation in the damaged zone.

To minimize the influence of fracture skin due to clay swelling, the effective stress at the fracture/matrix interface needs to be reduced while the strength of the unpropped fractures and cracks to hold the aperture open needs to be increased. This is illustrated in Figure 22 and 23, respectively. The effective stress at the fracture/matrix interface can be altered and hence the skin factor is reduced by increasing the salinity of the hydraulic fracturing water, for example by injecting KCl added water solution, which, in turn, will reduce the chemical imbalance between the clay-bound water in the matrix and fracturing water preventing osmosis and clay pore pressure build-up. In the absence of salinity adjustment, unfortunately the skin can increase to large values in the order of hundred with the increasing normalized effective stress at the fracture/matrix interface as shown in Figure 21. This is because clay swelling becomes so severe that the increase in the local stress due to clay pore pressure build-up may cause a significant reduction in the stress sensitive formation permeability (to almost a value of zero) leading to extremely large positive skin values and gas production rate to approach zero. This concept is illustrated in Figure 22 when the normalized effective stress at the fracture/matrix interface (d) approaches 0.9, the skin reaches

values in the order of hundred and a maximum value of approximately 840 when d is equal to 1 –

that is when there is complete closure of the unpropped fractures and cracks. These observations

highlight the severity of the damage that clay swelling may have on hydrocarbon (gas) production

in resource shales.

The resistance of the unpropped fractures and cracks to close is dependent on the formation

type. In Kim et al. (2019), the authors argue that the resistance can be improved by injecting

micro-proppants during hydraulic fracturing. Dahl et al. (2015) and Calvin et al. (2017) evaluated

the shale well production performance in the field by correlating the presence of microproppants

in the injected fracturing slurry to an increase in the production rate of the well.

Figure 23 indicates that the formations that are highly resistant to fracture closure tend to

have a lower fracture skin damage induced by clay swelling. This is because these formations can

resist the additional compressive stress due to osmotic pressure resulting from the diffusion of the

slick water molecules into the clay pores.

To minimize the contribution of capillary end effect (CEE) on the fracture skin, the average

water saturation in the damaged zone needs to be reduced as shown in Figure 24. This is also

achieved by increasing the salinity of slick water to prevent osmosis. Furthermore, it is worth

noting that the skin can increase to values in the order of hundred or thousand with the increasing

water saturation in the altered zone. This is because capillary end effect (CEE) can become so

severe that the gas saturation in the altered zone may reduce to almost the residual gas saturation

causing amplified water blockage. Consequently, the effective gas permeability approach to zero

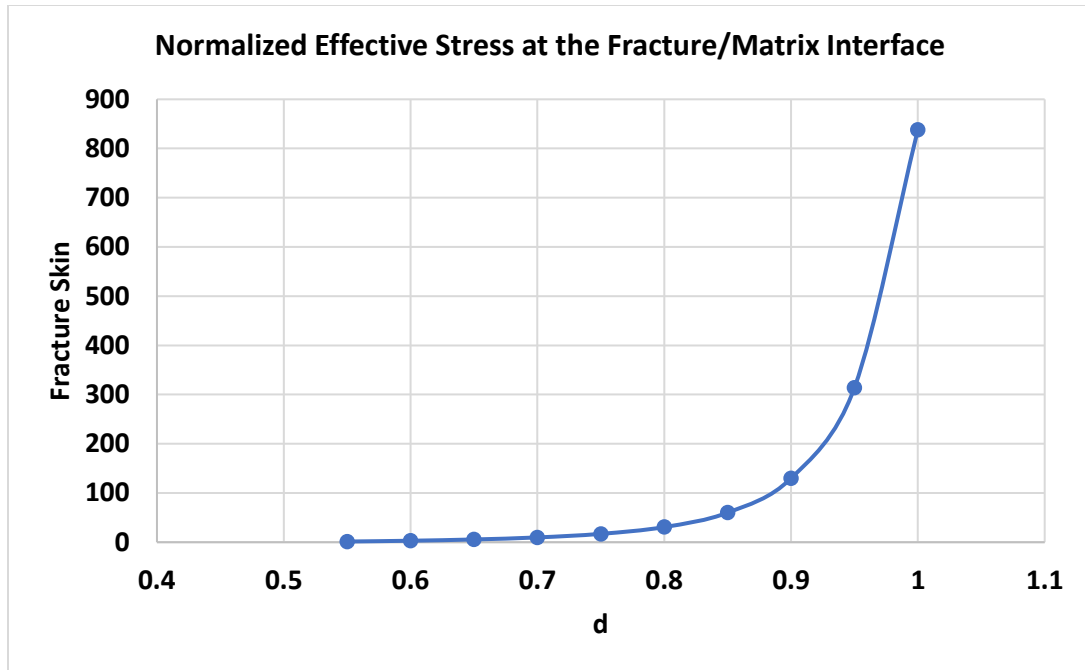and, hence, gas ceases to flow. This is illustrated in Figure 24 when the average water saturation

Figure 22. Plot of fracture skin as a function of the normalized effective stress at the fracture matrix/interface in the presence of clay swelling.
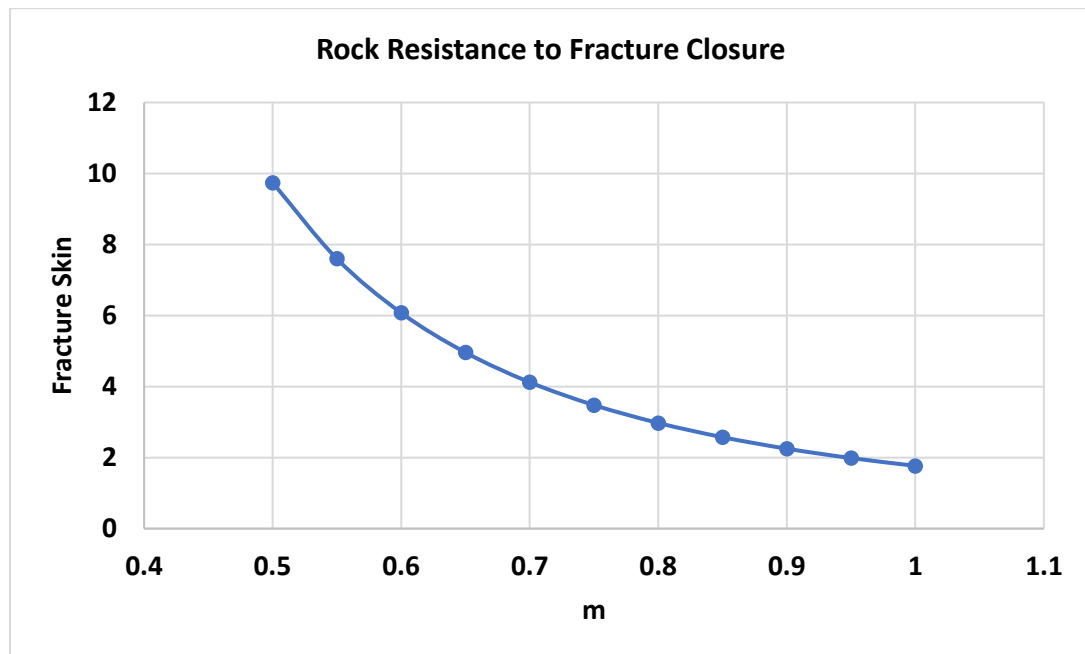

Figure 23. Plot of fracture skin as a function of the rock strength to hold the fracture open.
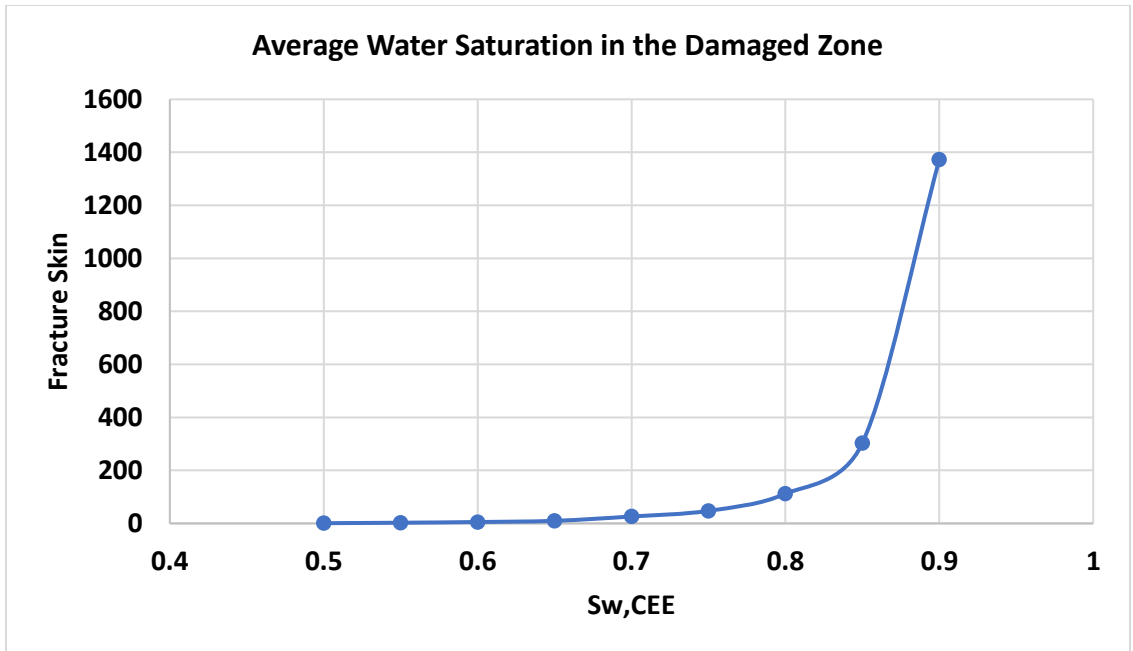
Figure 24. Plot of fracture skin as a function of the average water saturation in the damaged zone.

in the altered zone $(\overline{S_{w,CEE}})$ approaches 80 percent (0.8), the skin reaches values in the order of thousand and a maximum value of approximately 1400 at a water saturation of 0.9. This maximum damage skin occurs when the local gas saturation is reduced to the residual gas saturation and thus there will be no gas flow. This observed behavior highlights the severity of the damage that a case of extreme capillary end effect may have on hydrocarbon production in resource shales. Elputranto and Akkutlu (2018) previously argued that the CEE could be minimized by allowing the gas production at high rates. However, the impact of the initial (prior to injection) water saturation level on CEE damage is discussed here for the first time.

3.2. Sensitivity Analysis of Stimulation Skin

Next, I investigated the amount by which permeability of the altered zone needs to be improved through hydraulic fracturing operation to result in a net stimulation skin (negative skin). Figure 25 shows a positive fracture skin is decreasing when an improvement in permeability exists

due to unpropped fractures and cracks development during the hydraulic fracturing. However, this decrease is not at a high rate because the two other local physical and chemical phenomena associated with damage needs to be overcome. These two phenomena include: (1) high-stress due to slick water invasion and clay swelling effect, and (2) high water-saturation due to CEE. For the parameter values presented in table 1 in the previous section, I predict that the improvement in the formation permeability needs to be increased by a factor of 1.0 microdarcy to overcome the damage due to the combined effects of clay swelling and CEE – that is for the skin to reach a value of zero. Further improvement in permeability due to micro-proppants presence results in a net reservoir stimulation (negative fracture skin) as shown in Figure 25 and 26. However, it is worth noting that formation damage is more likely to occur and that net stimulation (negative skin) is more challenging to obtain. Interestingly, the negative skin seems to be bounded in these figures because further   improvement in permeability leads to skin approaching values of -2 asymptotically. These are illustrated in Figure 25-26 by the drastic increase in the damage skin (positive value) from a starting value of zero as the permeability in the altered zone is reduced, and a gentle increase in the stimulation skin (negative value) as the permeability in the altered zone is increased by similar amounts. These observations highlight the severity of the damage that clay swelling and CEE may have on hydrocarbon (gas) production in resource shales, and how imperative it is to adjust the salinity of the injected water and to keep the fractures and cracks in the matrix near the factures propped.

Using an improved matrix permeability (K_s) of 10 microdarcy along with the data shown in table 1, fracture skin was calculated. As shown in Figure 27, the cumulative fracture skin (S_{fD}) increases with increasing length of the altered zone (zone 2) whereas the gradient of the
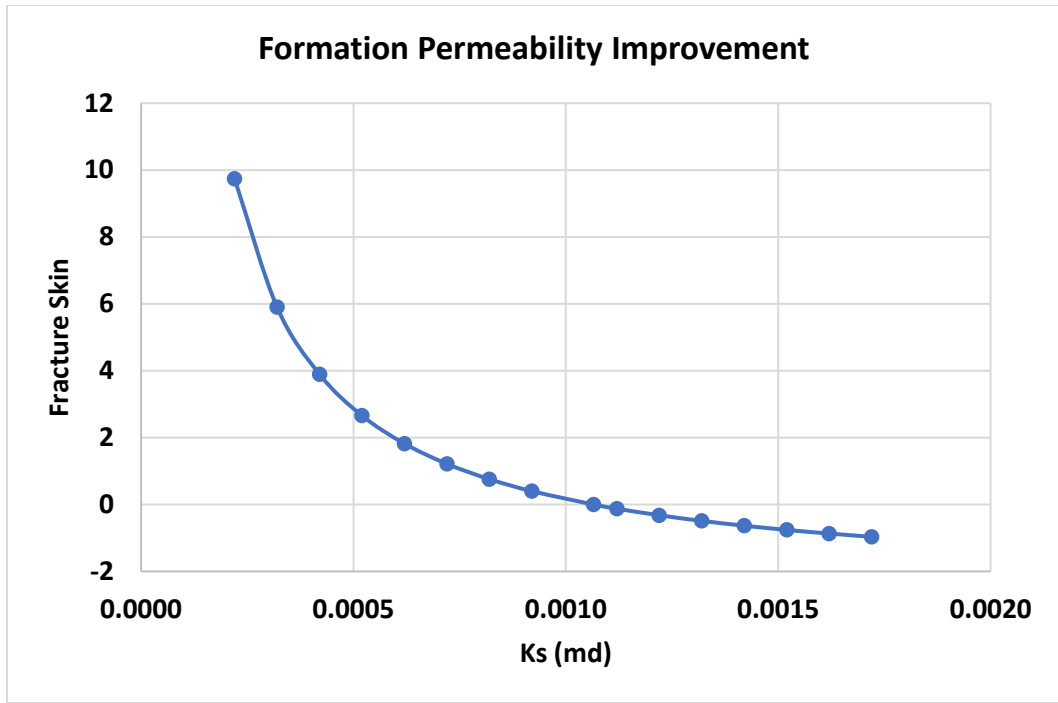
Figure 25. Plot of fracture skin as a function of improved permeability after fracturing.
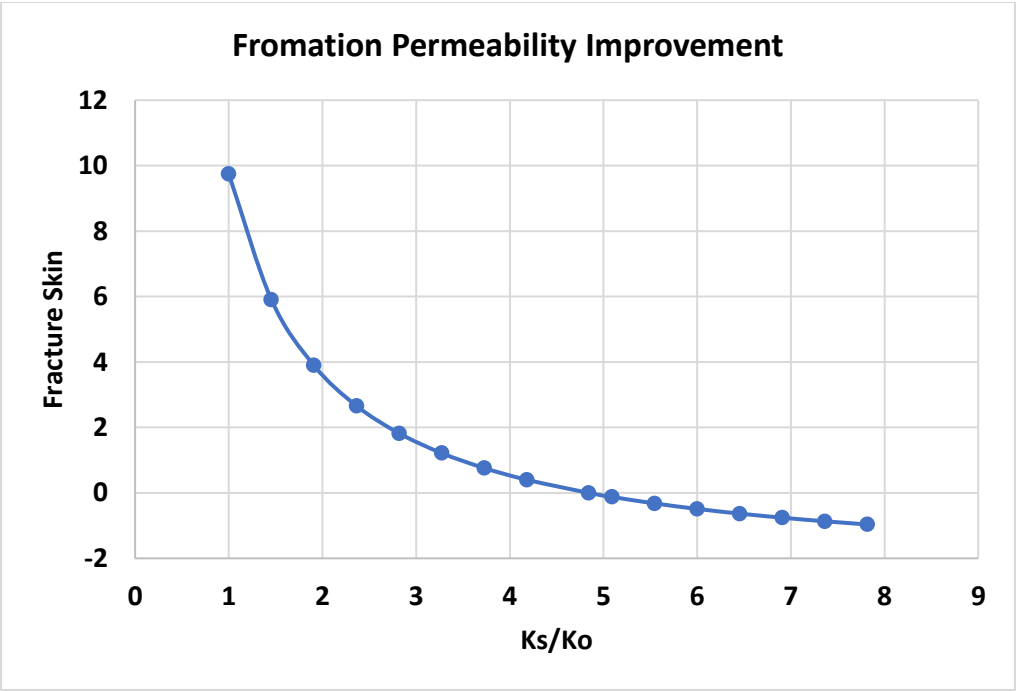

Figure 26. Plot of fracture skin as a function of the ratio of improved permeability due to unpropped fractures to initial permeability.
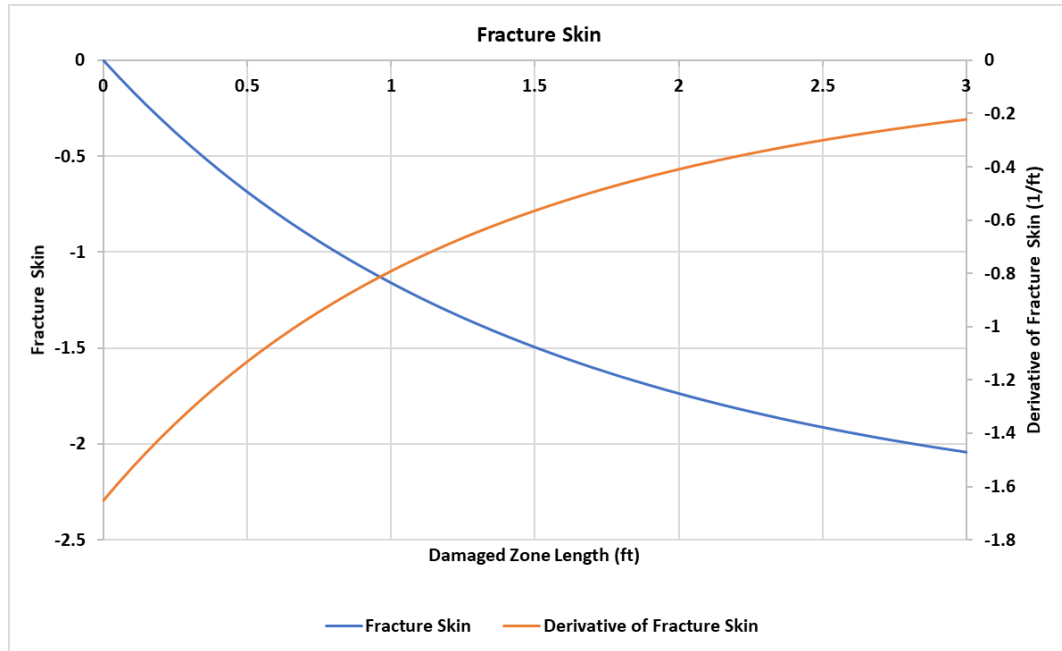
Figure 27. Plot of fracture skin as a function of the length of the damaged zone. The figure shows fracture skin increasing with increasing distance.

fracture skin decreases with increasing distance away from the fracture/matrix interface. This increase in the stimulation skin (large negative value) indicates the reduction in formation damage deeper into the rock formation, which mirrors the accumulation of water near the fracture/matrix interface and the increasing length of the region of improved permeability deeper into the formation.

3.3. Impact of CEE on Gas Production

To investigate the impact of the capillary end effect contribution to the damage fracture skin on gas production, a two-dimensional (620 x311 x 1) reservoir flow model is constructed using Eclipse. Additionally, the reservoir is assumed to be homogeneous and isotropic gas reservoir, and a stress-sensitive reservoir permeability model is considered. (This could be

accomplished by creating a stress sensitive permeability multiplier dataset as input for the simulator.) A multi-fracture horizontal well with 10 fractures is placed in the center of the reservoir as shown in Figure 28. The reservoir/fracture properties and well operating conditions used in the simulation are presented in table 2. To simulate the altered zone, a refined grid block of 4.13 feet is created near the fracture. These grid blocks are shown in red color in Figure 29. For the purpose of this study, permeability in the altered zone is considered to be equal to the formation permeability—that is to say no stimulation exists due to unpropped fracture or cracks on the face of the hydraulic fractures. CEE is simulated by defining a relative permeability function and irreducible water saturation for the altered zone different from the rest of the reservoir. To simulate increasing capillary end effect, multiple simulation runs are performed with varying water saturation in the altered zone: 20, 70, and 80 %.

Table 2. Reservoir properties and well operating conditions.

Formation Permeability (K)	0.00022 md
Formation Porosity (φ)	0.12
Initial Reservoir Pressure (P)	9000 psia
Irreducible Water Saturation (S_{wi})	0.1
Fracture Permeability (K_f)	5 Darcy
Rock Strength to hold aperture open (m)	0.5
Altered Zone Permeability (K_s)	0.00022 md
Bottom-hole Flowing Pressure (P_{wf})	2500 psia
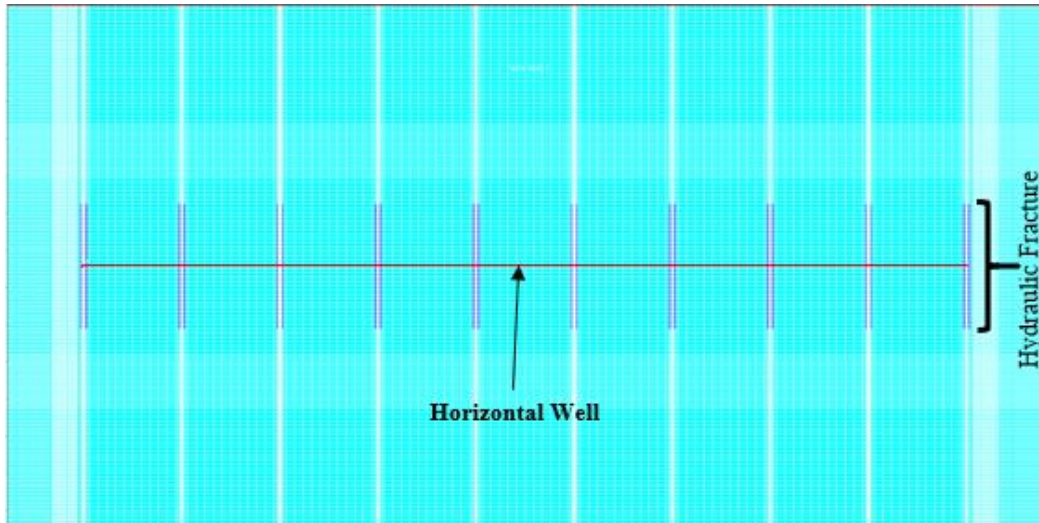
Figure 28. 2-dimensional (620 x 311 x 1) reservoir model constructed using Eclipse to simulate gas production from a horizonal well with 10 hydraulic fractures. The navy-blue lines represent the altered zone near each fracture; the red horizontal line represent the horizontal well, and cyan color grid blocks represent the reservoir.

Figure 29. Close-up view of a single fracture. The red vertical area represents the altered region on the face of the hydraulic fracture; the pink horizontal line represents a section of the horizontal well, and the black vertical line represents the hydraulic fracture.

39

As shown in Figure 30 and 31, the simulated gas production rate and cumulative gas production decrease with increasing water saturation in the damaged/altered zone. As previously discussed, this is because as the CEE is amplifi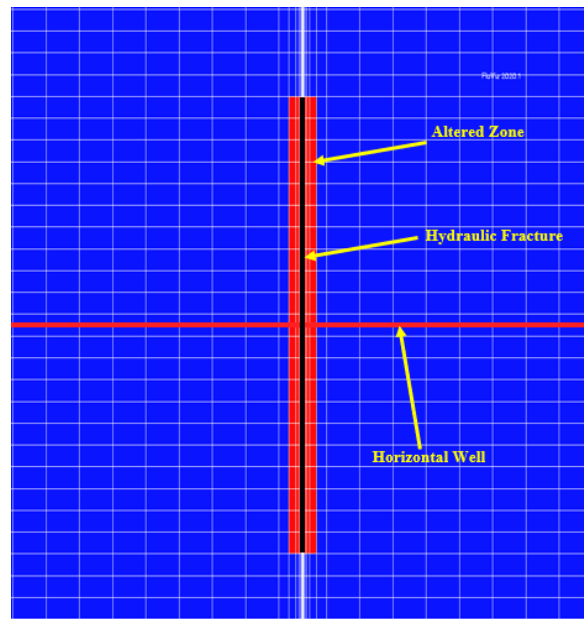ed due to strong capillarity in the formation matrix, more water will tend to accumulate near the fracture/matrix interface resulting in a decrease in the local gas saturation in the altered zone. Consequently, the gas relative permeability and gas production rate will decrease as well. Depending on the severity of the capillary end effect, the gas saturation in the altered zone may reduce to almost the residual gas saturation leading to amplified water blockage and/or total loss of gas flow. This is illustrated in Figure 30 when the average water saturation in the altered zone ($\overline{S_{w,CEE}}$) reaches 80 percent (0.8), the gas production rate decreases from 5 MMSCF (when $\overline{S_{w,CEE}} = 0.2$) to 1 MMSCF after 10 days
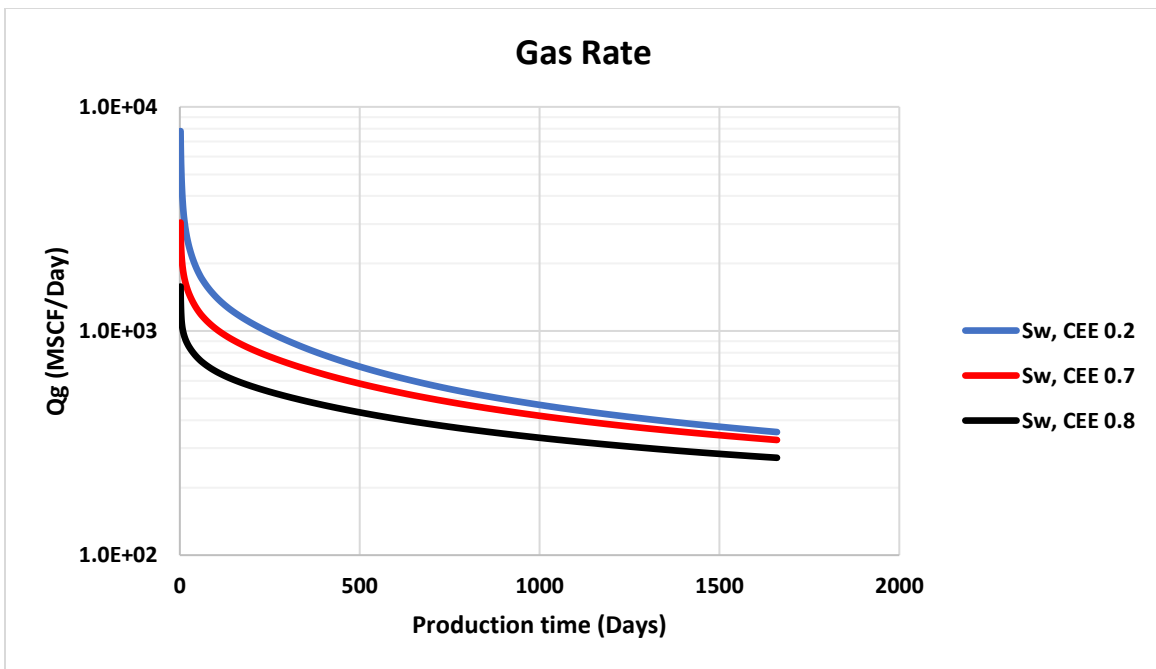

Figure 30. Comparative plot of gas production rate during 4.5 years of production shows that gas rate decreases with increasing water suturing in the damaged/altered zone.
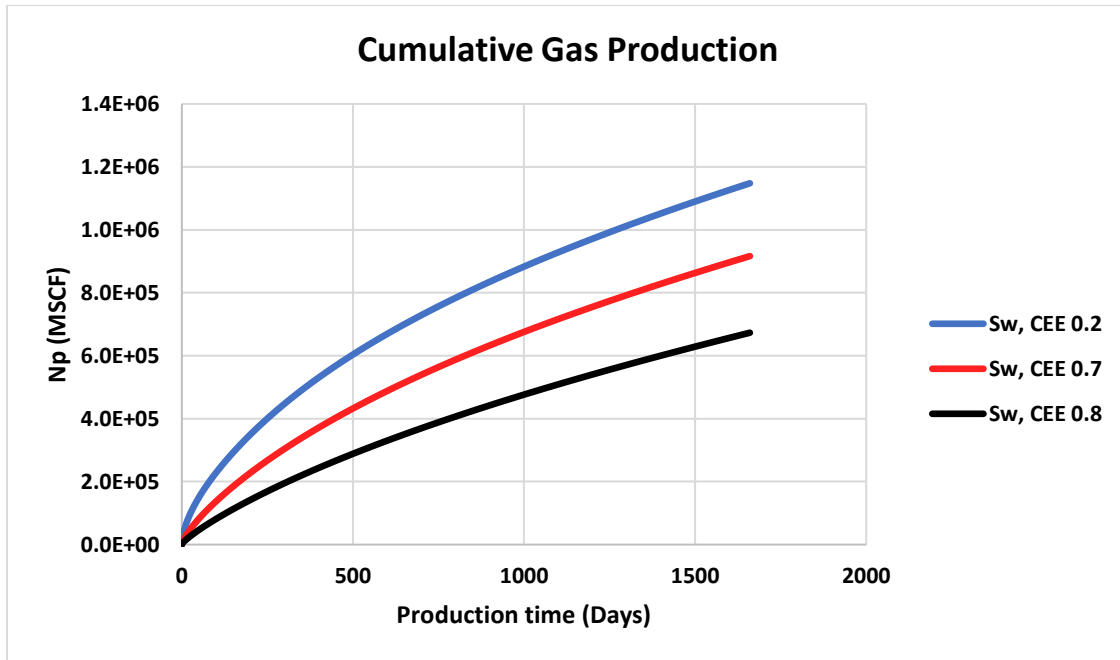
Figure 31. Comparative plot of cumulative gas production during 4.5 years of production shows that cumulative gas volume decreases with increasing water saturation in the damaged/altered zone.

of production. Additionally, the cumulative gas production decreases from 1.15 BSCF (when $\overline{S_{w,CEE}} = 0.2$) to 670 MMSCF (when $\overline{S_{w,CEE}} = 0.8$) after a production period of 4.5 years, which represents a 41 percent decrease in the gas production. The simulation results validate the fracture skin model prediction of increasing damage skin with increasing water saturation in the altered zone and further highlight the severity of the negative impact that capillary end effect (CEE) may have on gas production in resource shales.

3.4. Impact of Clay Swelling on Gas Production

Next, the impact of clay swelling (i.e., a component of the fracture damage skin) on gas production is investigated. The 2-D (areal) reservoir model presented in the previous section is

used and the water saturation in the altered zone is set to a constant value of 40 percent to simulate CEE. As presented in equation 20, a stress sensitivity permeability model is used to model the increasing effect of clay swelling on gas production. Because the normalized effective stress at the fracture/matrix interface when clay swelling develops in the altered zone (d) is the most sensitivity geo-mechanical parameter controlling the damage skin, four (4) cases of d are considered: 0.345, 0.305, 0.265,0.225. It should also be noted that the permeability in the altered zone is considered to be equal to the formation permeability at zero effective stress — that is to say there is no stimulation due to unpropped fracture or cracks on the face of the hydraulic fractures. The corresponding normalized effective stress functions and permeability multipliers (i.e., the term multiplying the formation permeability at zero effective stress presented in equation 20) are presented in Figure 32 and 33. As previously discussed, the normalized effective stress increases
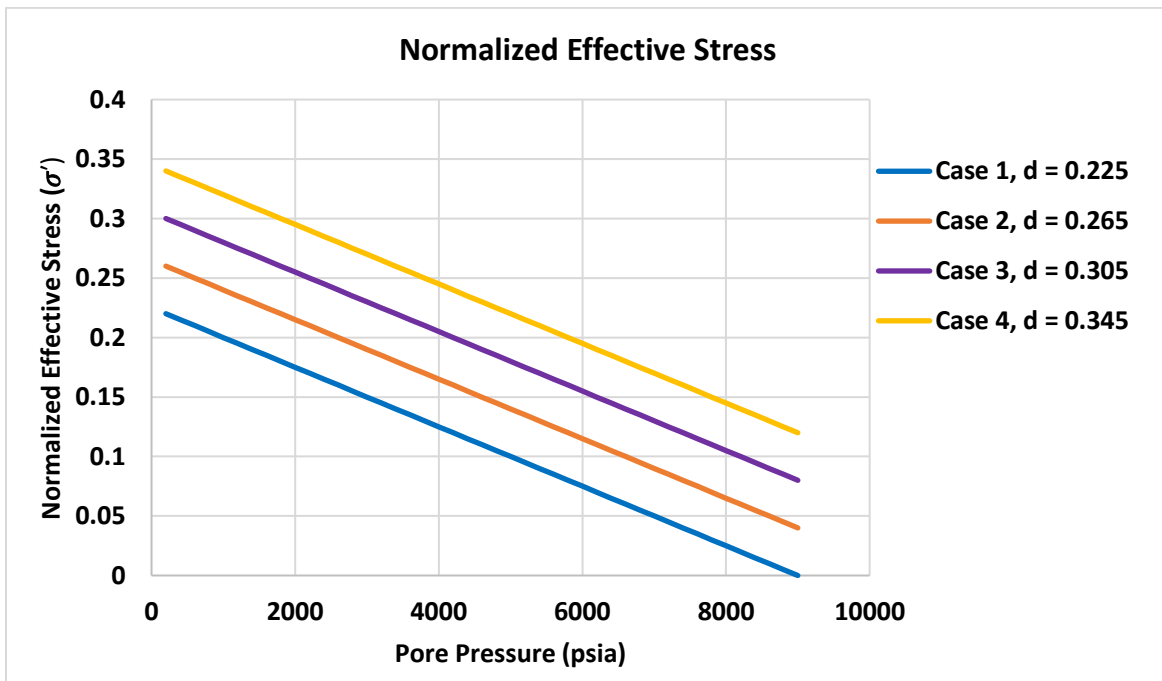

Figure 32. Comparative plot of the normalized effective stress a function of pore pressure with varying normalized effective stress at the fracture/matrix interface.
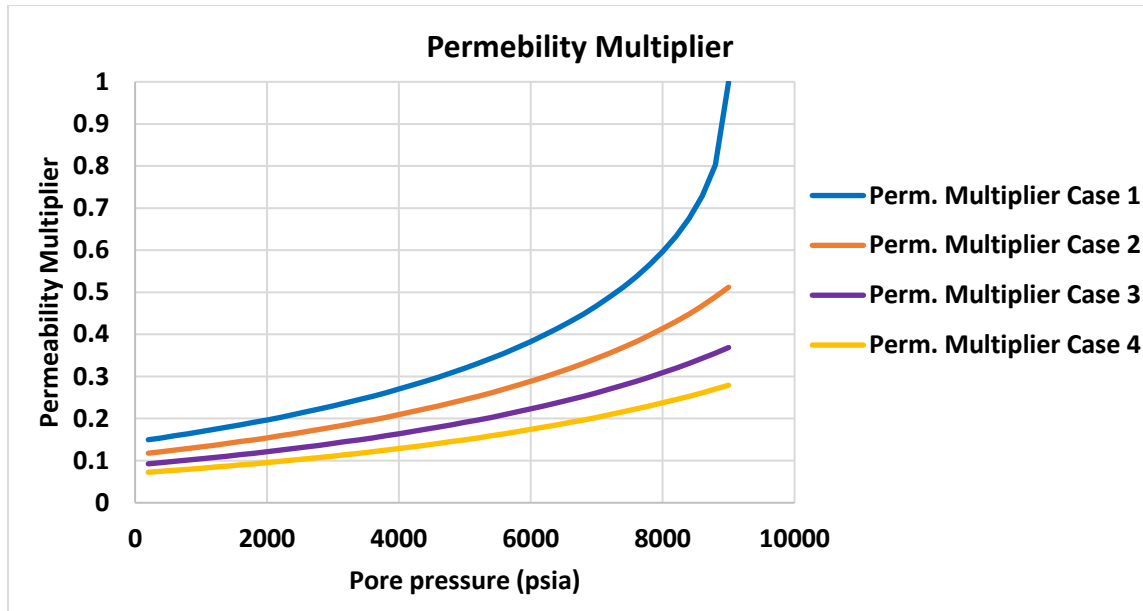
Figure 33. Comparative plot of permeability multiplier as a function of pore pressure with varying normalized effective stress at the fracture/matrix interface.

with decreasing distance away from the fracture/matrix interface. This is because as the fluid (gas) approaches the fracture/matrix interface, pore pressure decreases while osmotic pressure increases as water tends to accumulate near the interface due to the combined effect of CEE and osmosis. The two opposite phenomena lead to a net increase in the compressive stress, which in turn add to the overburden pressure.

As shown in Figure 34 and 35, gas production rate and thus cumulative gas production decrease with increasing normalized effective stress at the fracture/matrix interface when clay swelling develops in the altered zone. As previously discussed, this is because of the chemical imbalance (difference in salinity) between the clay-bound water and slick water leading to the diffusion of slick water molecules into the clay pores and causing an increase in the local stress due to clay pore pressure build-up as a result. Depending on the severity of clay swelling the
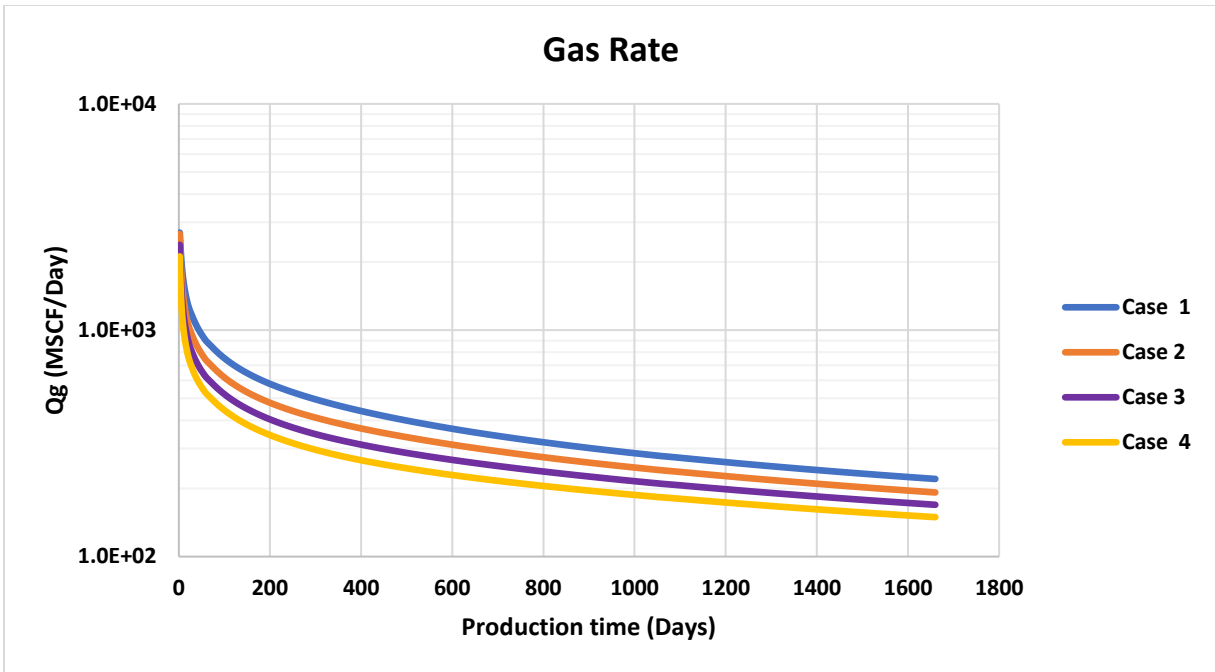
43

Figure 34. Comparative plot of gas production rate during 4.5 years of production shows that gas rate decreases with increasing normalized effective stress.
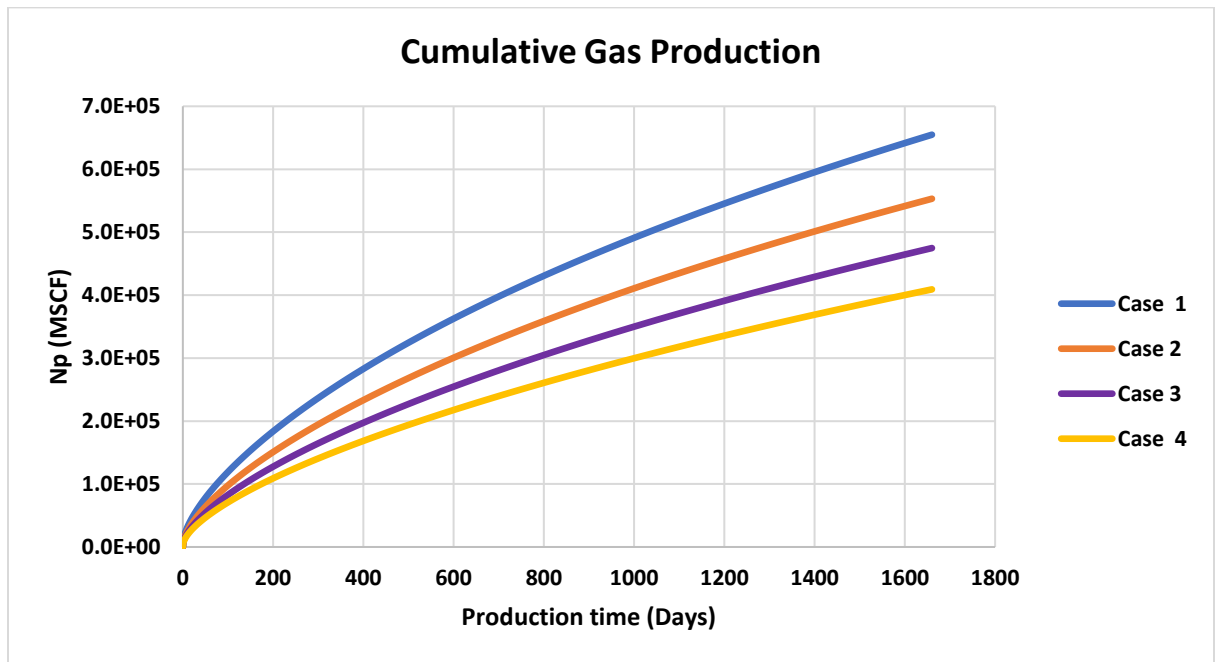

Figure 35. Comparative plot of cumulative gas production during 4.5 years of production shows that the cumulative gas volume decreases with increasing normalized effective stress.

increase in the local stress due to clay pore pressure build-up may cause a significant reduction in the stress sensitive formation permeability or complete closure of the unpropped fractures and cracks on the face of the hydraulic fractures. This in turn translates to significantly reduced gas production rates or complete loss of gas production. This is illustrated in Figure 34 when the normalized effective stress at the fracture/matrix interface reaches 0.345, the gas production rate decreases from 1.6 MMSCF (when d = 0.225 in Case 1) to 1.0 MMSCF after 10 days of production. Additionally, the cumulative gas production decreases from 655 MMSCF (when d = 0.225) to 409 MMSCF (when d = 0.345) after a production period of 4.5 years, which represents a 38 percent decrease in the gas production. The simulation results corroborate the fracture skin model prediction of increasing damage skin with increasing normalized effective stress at the fracture/matrix interface and further highlight the severity of the negative impact that clay swelling may have on gas production in resource shales.

Because the damage associated with clay swelling is due to osmotic pressure, it is paramount to establish a constitutive relationship between the parameter controlling clay pore/osmotic pressure build-up. Eveline et al. (20017) argued that osmotic pressure is mainly controlled by salt mass fraction (salt concentration) between two fluids and that the transfer of ions from the low salt concentration fluid to the high salt concentration fluid is limited by the clay membrane efficiency. In this study, theoretical description of osmosis follows chemical osmosis model developed by Bader and Kooi (2005), which assumes the two driving forces of the mass flux are the hydraulic pressure and the chemical potential gradients. The proposed model has been derived for an aqueous phase with single solute species and the osmotic pressure is given by:

$$\pi = \upsilon \, R \, T \frac{\rho_f}{M_s} \mathcal{R} \, \nabla x^s \qquad\qquad 43$$

Here v is the dissociation coefficient for the salt dissociating into ions ($v = 2$ for NaCl), ∇x^s is the salt mass fraction difference, R is the universal gas constant, T is temperature, ρ_f is the fluid density, M_s is the salt molar mass and $\mathcal{R}$ is the membrane efficiency.

To investigate the effect of membrane efficiency and salt mass fraction difference between two fluids, a container holding two aqueous solutions with different salt concentration separated by a semi-permeable membrane is considered. The container has an initial pressure of 1,450 psia and temperature of 100 ∘C. The associated pressure increase (osmotic pressure) in the side of the semi-permeable membrane containing higher salt concentration is calculated using equation 43. The estimated osmotic pressure corresponding to varying membrane efficiency and salt mass fraction difference is shown in Figure 36. It can be observed that osmotic pressure increases with increasing salt mass fraction difference (difference in salinity) and clay membrane efficiency.
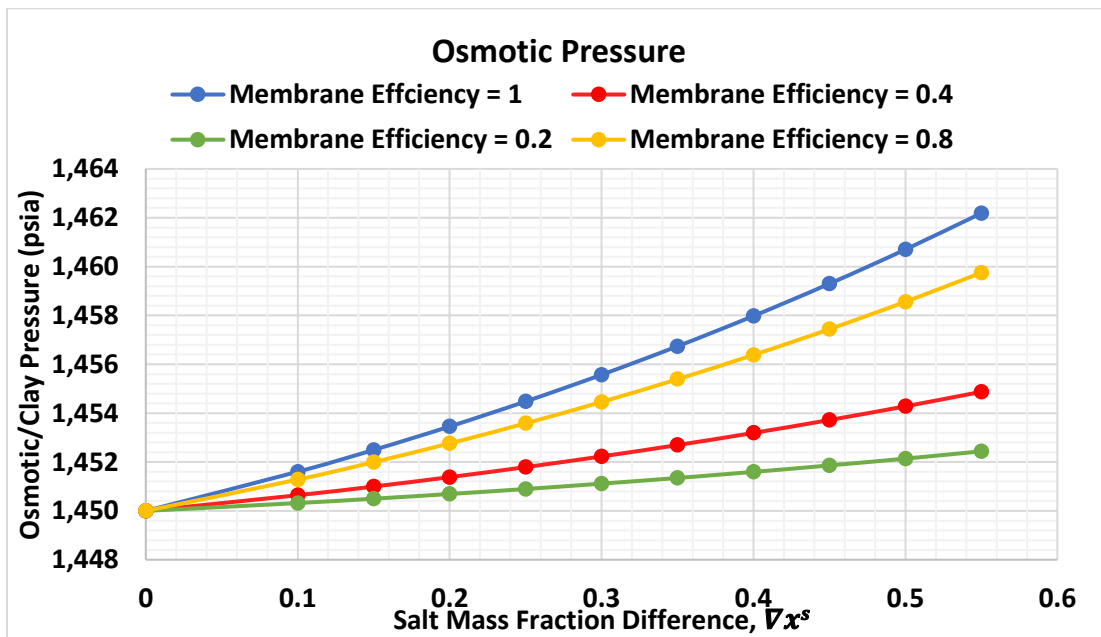

Figure 36. Comparative plot of osmotic pressure as a function of salt mass fraction difference shows that osmotic pressure increases with increasing clay membrane efficiency and salt mass fraction difference.

3.5. Impact of Improved Formation Permeability in the Altered Zone on Gas Production

The impact of enhanced permeability in the altered zone on gas production is investigated next. The 2-D (areal) reservoir model presented in section 4.3 is used, the water saturation in the altered zone is set to a constant value of 70 percent to simulate CEE and the hydraulic fracture permeability is set to 10 millidarcy. Additionally, the permeability multiplier function used in Case 1 from the clay swelling study is considered as the permeability model outside of the altered zone in this study. To account for clay swelling, the permeability multiplier function used in Case 2 from the clay swelling study is considered as the permeability model in the altered zone. Three (3) cases of improved permeability are considered: In Case 1, the permeability is assumed to be twice the formation matrix permeability ($K_s = 2\,K_0$). In Case 2, and 3, the permeability is assumed to be 10 and 20 times the matrix permeability, respectively.

As shown in Figure 37 and 38, gas production rate and thus cumulative gas production increases with increasing permeability in the altered zone. As previously discussed, this is because when there is improvement in permeability due to unpropped fractures and cracks development during hydraulic fracturing, fracture skin damage decreases as the two local physical and chemical phenomena associated with damage are overcome. The two phenomena include: (1) high-stress due to slick water invasion and clay swelling effect, and (2) high water-saturation due to capillary end effect. However, it should be noted that the gas production rate and thus cumulative gas production increase until the improved permeability in the altered zone reaches a value after which further improvement in the permeability does not results in a significant improvement in the gas production rate. This is illustrated in Figure 37 and 38 when the altered zone permeability becomes 10 times larger than the matrix permeability, further improvement in permeability merely improves the gas production.
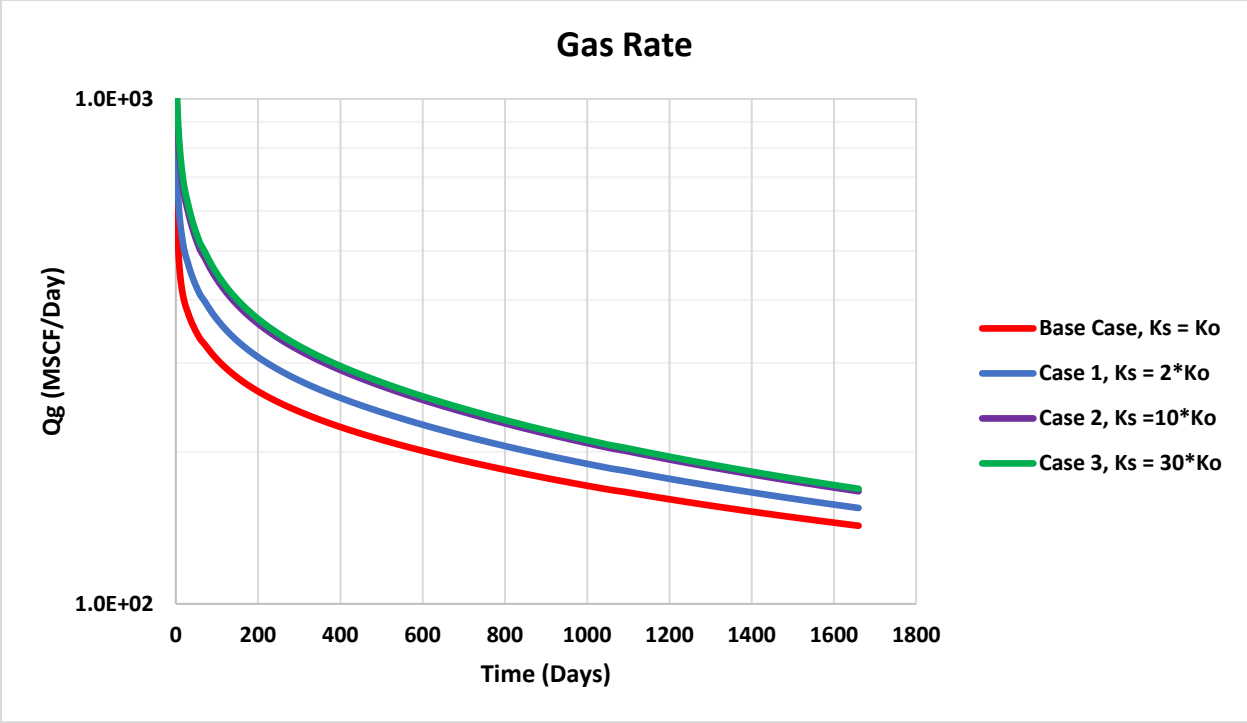
Figure 37. Comparative plot of gas production rate during 4.5 years of production shows that gas rate increases with increasing permeability in the altered zone.
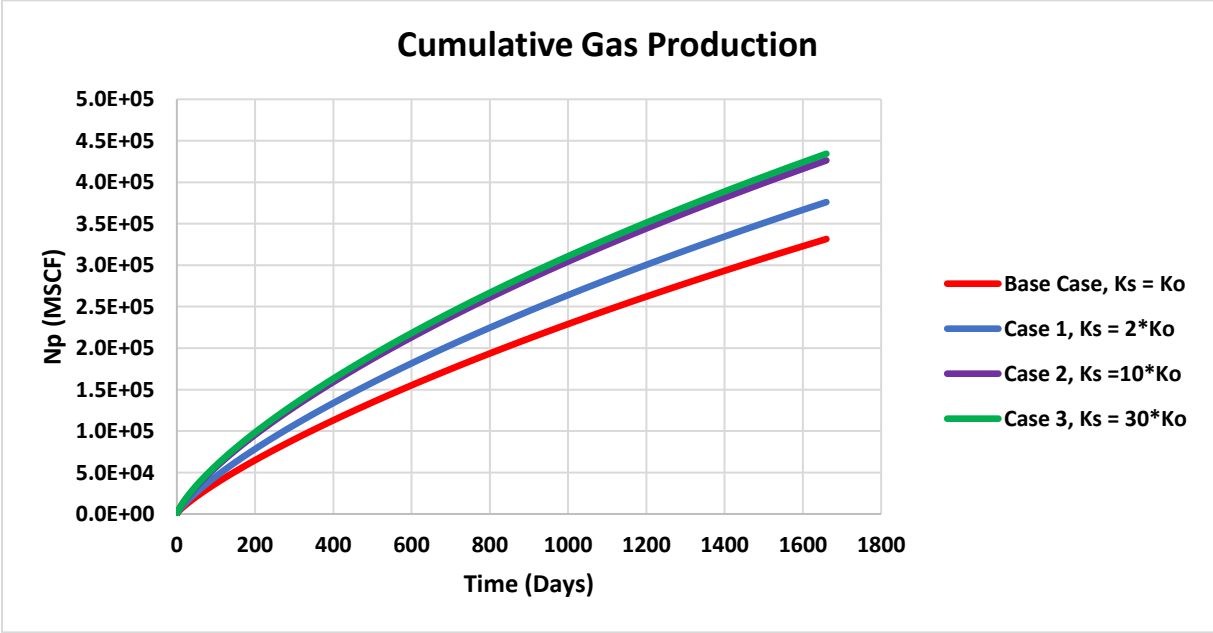

Figure 38. Comparative plot of cumulative gas production during 4.5 years of production shows that the cumulative gas volume increases with increasing permeability in the altered zone.

To investigate the decreasing effect of improved permeability in the altered zone on gas production, the fracture skin is calculated for one of the grid blocks (grid 161,150,1) at the fracture/matrix interface using equation 41. Here, the fracture half-length denoted by x_f in the fracture skin equation corresponds to the length of the grid block (5 ft) in the j-direction. The grid block water saturation and corresponding relative permeability in the altered zone are directly extracted from the reservoir simulator. The base case simulation results correspond to the grid block properties in the absence of alterations whereas the simulation results of the three cases of improved permeability correspond to the grid block properties in the presence of alterations.

In Equation 41, the terms under the first summation sign are the change in permeability (permeability multiplier) in the absence of alterations, which corresponds to the base case. On the other hand, the terms under the second summation sign represent the change in permeability (permeability multiplier) in the presence of alteration, which corresponds to any of the improved permeability cases (Case 1 through 3). These permeability multipliers are also directly extracted from the reservoir simulator.

As shown in Figure 39, the negative skin increases with increasing altered zone permeability, and it appears to be bounded as further improvement in permeability leads to the skin approaching a value of − 0.18 asymptotically. This observed behavior validates the skin behavior predicted by the proposed skin model as previously shown in Figure 25.
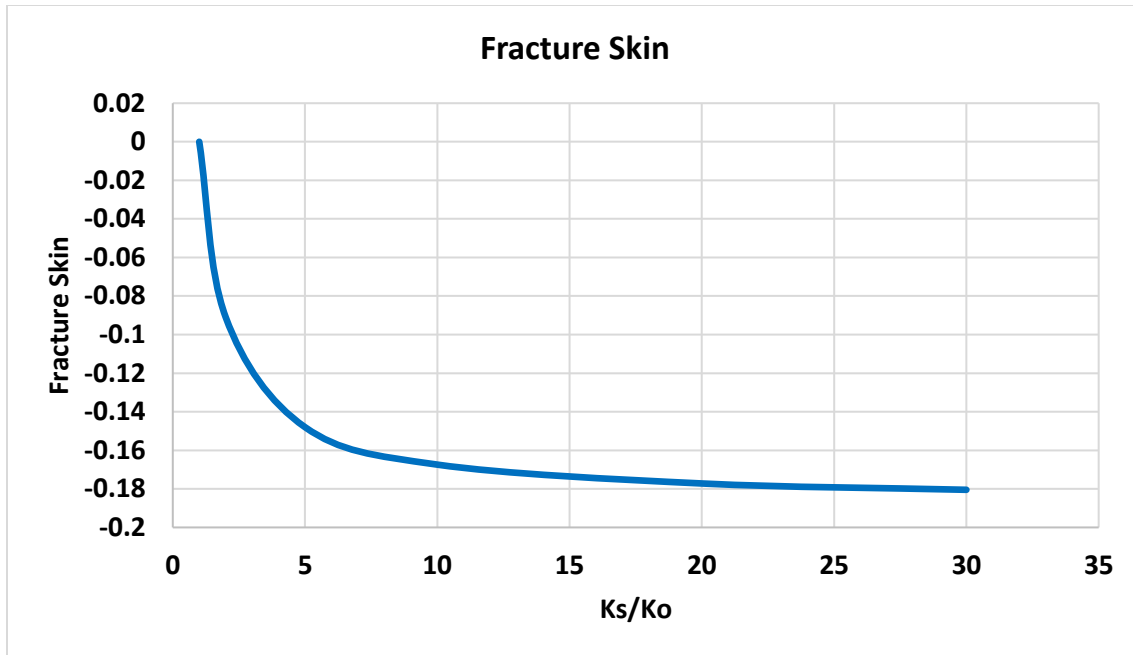
Figure 39. Plot of the simulated fracture skin as a function of the ratio of improved permeability due to unpropped fractures to initial permeability at the end of a 4.5-year gas production period.

3.6. Time Dependence of Fracture Skin

Lastly, I investigated the behavior of fracture skin as a function of production time. To this end, the fracture skin is computed for 120 days of gas production using equation 41 as described in the previous section. Three (3) cases of fracture skin are studied: In Case 1, the computed fracture skin is the difference in pressure drop between the Base Case and Case 1 (where the altered zone permeability is twice the matrix permeability) as described in section 4.5. In Case 2, the computed fracture skin is still the difference in the pressure drop between the Base Case and Case 1. However, CEE is assumed to be nonexistent. In Case 3, the fracture skin is computed similarly, but this time both CEE and clay swelling are assumed to be negligible.

50

As shown in Figure 40, the blue curve corresponds to the fracture skin when both CEE and clay swelling develop in the altered zone whereas the red dashed line denotes the fracture skin in the absence of both CEE and clay swelling. Furthermore, the purple dashed line denotes the fracture skin in the absence of CEE. Figure 40 shows that the fracture skin (blue line) is initially large and constant during the first few minutes of production time. This period can be associated with the flowback period where the fluid present in the hydraulic fractures is produced and lasts for approximately 0.01 days (14.5 minutes). This flowback period is followed by the gas production period which is marked by a gradual reduction of the fracture skin. This reduction in the fracture skin can be attributed to the two damage mechanisms previously discussed, namely CEE and clay swelling. It is worth noting that the gas production period is divided into two periods: the stimulation period and damage period. During the stimulation period, the effect of improved permeability due to unpropped fractures and cracks dominates the damage due to the combined effects of CEE and clay swelling. This period is thus marked by a negative fracture skin (net stimulation). On the other hand, the damage period is marked by a positive fracture skin, and this is when CEE and clay swelling overcome the permeability improvement due to the secondary unpropped fractures and cracks. This reduction in the fracture skin can vary depending on the severity of the damage associated with CEE and clay swelling

Additionally, it can be observed that in the absence of alterations due to CEE or/and clay swelling, the fracture skin is significantly large. As shown in Figure 40, the fracture skin has an initial value of approximately -0.2 when CEE or/and clay swelling are considered. During the flow black period, Case 2 and Case 3 have approximately the same fracture skin because only the fluid present in the hydraulic fractures is being produced. At the onset of the gas production period (at 0.01 days), the fracture skin begins to decrease. In Case 2, the fracture skin (red dashed line)

51

reduction is due to the combined effects of clay swelling and reduction in pore pressure due to gas production. On the other hand, the reduction in the fracture skin in Case 3 is due solely to the reduction in pore pressure as gas is produced.
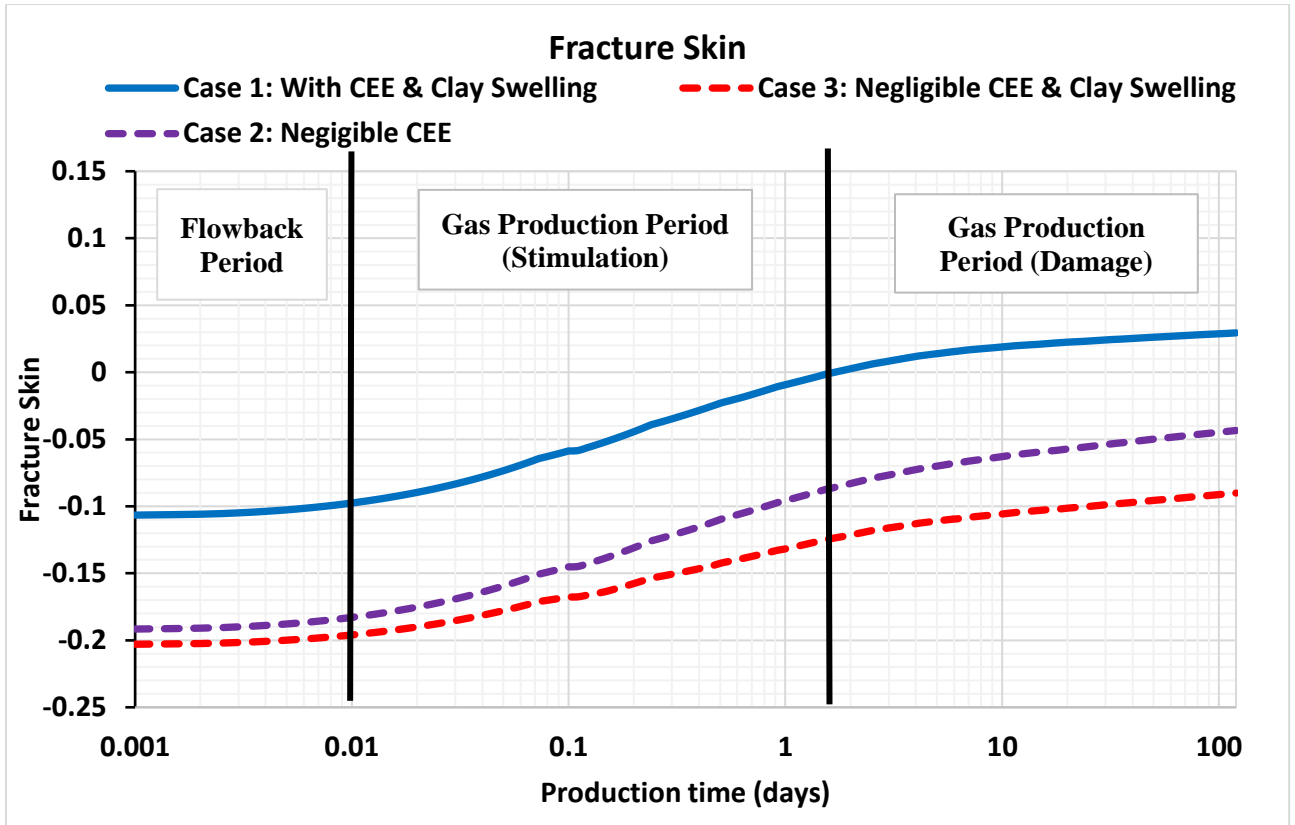

Figure 40. Semi-log plot of the simulated fracture skin as a function of production time. The blue line denotes the fracture skin when both CEE and clay swelling develops in the altered zone. The red dashed line denotes the fracture skin in the absence of CEE and clay swelling.

4. CONCLUSIONS

A fracture skin model was proposed and explicitly includes local physical and chemical phenomena resulting from the hydraulic fracturing of the reservoir (i.e., resource shales) and the interaction of the fracturing fluid with the reservoir. The following observations are made at the end of this study:

1. Fracture skin increases at a decreasing rate with distance away from the fracture/matrix interface, which mirrors the invaded water near the fracture/matrix interface.

2. Clay swelling is the predominant damage mechanism and is controlled by the geo-mechanical parameters of the permeability model: (1) the normalized effective stress at the fracture/matrix interface when clay swelling develops in the altered zone, and (2) strength of the secondary unpropped fractures and cracks inside the damage zone to stay open.

3. The contribution of the capillary-end-effect to the skin is mainly controlled by the average water saturation in the damaged zone. Capillary-end-effect can thus be severe in formations that have high water saturation.

4. Formation damage is reduced by increasing the salinity of the injected water, which in turn reduces the chemical imbalance between the clay-bound water and the fracturing fluid preventing osmosis.

5. When there is significant improvement in permeability due to unpropped fracture and crack development during fracturing, the damage mechanism associated with clay swelling and capillary end effect may become insignificant.

6. Formation damage is more likely to occur while a net fracture stimulation (negative skin) is more challenging to obtain.

5. REFERENCES

Bader, S. and Kooi, H. 2005. Modelling of solute and water transport in semi-permeable clay membranes: comparison with experiments. *Advances in Water Resources* **28** (3): 203-214. http://dx.doi.org/10.1016/j.advwatres.2004.11.001.

Calvin, J., Grieser, B., and Bachman, T. 2017. Enhancement of Well Production in the SCOOP Woodford Shale through the Application of Microproppant. Presented at the SPE Hydraulic Fracturing Technology Conference and Exhibition, The Woodlands, Texas, USA, January 24–26, 2017, https://doi.org/10.2118/184863-MS.

Dahl, J., Nguyen, P., Dusterhoft, R. et al. 2015. Application of Micro-Proppant to Enhance Well Production in Unconventional Reservoirs : Laboratory and Field Results. Presented at the SPE Western Regional Meeting, Garden Grove, California, USA, April 27–30, 2015, https://doi.org/10.2118/174060-MS.

Elputranto, R. and Akkutlu, I. Y. 2020. Near-Fracture Capillary End Effect on Shale-Gas and Water Production. *SPE J.* **25** (04): 2041-2054. https://doi.org/10.2118/201092-PA.

Elputranto, R., Cirdi, A. P., and Akkutlu, I. Y. 2020. Formation Damage Mechanisms Due to Hydraulic Fracturing of Shale Gas Wells. Presented at the SPE Europec, Virtual, December 1–3, 2020, https://doi.org/10.2118/200582-MS.

Eveline, V. F., Akkutlu, I. Y., and Moridis, G. J. 2016. Impact of Hydraulic Fracturing Fluid Damage on Shale Gas Well Production Performance. Presented at the SPE Annual Technical Conference and Exhibition, Dubai, UAE, September 26–28, 2016, https://doi.org/10.2118/181677-MS.

Eveline, V., Akkutlu, I., and Moridis, G. 2017. Numerical Simulation of Hydraulic Fracturing Water Effects on Shale Gas Permeability Alteration. *Transport in Porous Media* **116** (2): 727-752. http://dx.doi.org/10.1007/s11242-016-0798-4

Gangi, A. 1978. Variation of whole and fractured porous rock permeability with confining pressure. *International Journal of Rock Mechanics and Mining Sciences & Geomechanics Abstracts* **15** (5): 249-257. http://dx.doi.org/10.1016/0148-9062(78)90957-9.

Guo, B., Gao, D., and Wang, Q. 2011. The Role of Formation Damage in Hydraulic Fracturing Shale Gas Wells. Presented at the SPE Eastern Regional Meeting, Columbus, Ohio, USA, August 17–19, 2011, https://doi.org/10.2118/148778-MS.

Gupta, R. and Maloney, D. R. 2014. Intercept Method - A Novel Technique to Correct Steady-State Relative Permeability Data for Capillary End-Effects. Presented at the Abu Dhabi International Petroleum Exhibition and Conference, Abu Dhabi, UAE, November 10–13, 2014, https://doi.org/10.2118/171797-MS.

Kim, B. Y., Akkutlu, I. Y., Martysevich, V. et al. 2019. Monolayer Microproppant-Placement Quality Using Split-Core-Plug Permeability Measurements Under Stress. *SPE J.* **24** (04): 1790-1808. https://doi.org/10.2118/189832-PA.